

SHORT REPORTS

ACE2-containing defensosomes serve as decoys to inhibit SARS-CoV-2 infection

Krystal L. Ching¹, Maren de Vries², Juan Gago^{2,3}, Kristen Dancel-Manning^{4,5}, Joseph Sall^{4,5}, William J. Rice^{4,6}, Clea Barnett⁷, Alireza Khodadadi-Jamayran^{8,9}, Aristotelis Tsirigos^{8,9,10}, Feng-Xia Liang^{4,5}, Lorna E. Thorpe³, Bo Shopsis^{2,11,12}, Leopoldo N. Segal⁷, Meike Dittmann^{2*}, Victor J. Torres^{2,12*}, Ken Cadwell^{1,2,13*}

1 Kimmel Center for Biology and Medicine at the Skirball Institute, New York University Grossman School of Medicine, New York, New York, United States of America, **2** Department of Microbiology, New York University Grossman School of Medicine, New York, New York, United States of America, **3** Division of Epidemiology, Department of Population Health, New York University Grossman School of Medicine, New York, New York, United States of America, **4** Division of Advanced Research Technologies, New York University Langone Health, New York, New York, United States of America, **5** The Microscopy Laboratory at New York University Langone Health, New York, New York, United States of America, **6** The Cryo-Electron Microscopy Laboratory at New York University Langone Health, New York, New York, United States of America, **7** Division of Pulmonary and Critical Care Medicine, New York University Grossman School of Medicine, New York, New York, United States of America, **8** Department of Pathology, New York University School of Medicine, New York, New York, United States of America, **9** Applied Bioinformatics Laboratories, NYU School of Medicine, New York, New York, United States of America, **10** Perlmutter Cancer Center, NYU Langone Health, New York, New York, United States of America, **11** Division of Infectious Diseases and Immunology, Department of Medicine, New York University Grossman School of Medicine, New York, New York, United States of America, **12** Antimicrobial-Resistant Pathogens Program, NYU Langone Health, New York, New York, United States of America, **13** Division of Gastroenterology and Hepatology, Department of Medicine, New York University Grossman School of Medicine, New York, New York, United States of America

* Meike.Dittmann@nyulangone.org (MD); Victor.torres@nyulangone.org (VJT); ken.cadwell@nyulangone.org (KC)



OPEN ACCESS

Citation: Ching KL, de Vries M, Gago J, Dancel-Manning K, Sall J, Rice WJ, et al. (2022) ACE2-containing defensosomes serve as decoys to inhibit SARS-CoV-2 infection. *PLoS Biol* 20(9): e3001754. <https://doi.org/10.1371/journal.pbio.3001754>

Academic Editor: Eng Eong Ooi, Duke-NUS: Duke-NUS Medical School, SINGAPORE

Received: December 19, 2021

Accepted: July 12, 2022

Published: September 13, 2022

Copyright: © 2022 Ching et al. This is an open access article distributed under the terms of the [Creative Commons Attribution License](https://creativecommons.org/licenses/by/4.0/), which permits unrestricted use, distribution, and reproduction in any medium, provided the original author and source are credited.

Data Availability Statement: All relevant data are within the paper and its [Supporting Information](#) files.

Funding: This work was in part funded by National Institutes of Health (NIH) grants DK093668 (K.C.), HL123340 (K.C.), AI130945 (K.C.), AI140754 (K.C.), DK124336 (K.C.), AI121244 (K.C. and V.J.T.), AI099394 (V.J.T.), AI105129 (V.J.T.), AI137336 (V.J.T.), AI133977 (V.J.T.), AI140754 (V.J.T.), AI149350 (V.J.T.), AI143639 (M.D.), AI139374 (M.D.), CA244775 (L.N.S., NCI/NIH). Further funding

Abstract

Extracellular vesicles of endosomal origin, exosomes, mediate intercellular communication by transporting substrates with a variety of functions related to tissue homeostasis and disease. Their diagnostic and therapeutic potential has been recognized for diseases such as cancer in which signaling defects are prominent. However, it is unclear to what extent exosomes and their cargo inform the progression of infectious diseases. We recently defined a subset of exosomes termed defensosomes that are mobilized during bacterial infection in a manner dependent on autophagy proteins. Through incorporating protein receptors on their surface, defensosomes mediated host defense by binding and inhibiting pore-forming toxins secreted by bacterial pathogens. Given this capacity to serve as decoys that interfere with surface protein interactions, we investigated the role of defensosomes during infection by Severe Acute Respiratory Syndrome Coronavirus 2 (SARS-CoV-2), the etiological agent of Coronavirus Disease 2019 (COVID-19). Consistent with a protective function, exosomes containing high levels of the viral receptor ACE2 in bronchoalveolar lavage fluid (BALF) from critically ill COVID-19 patients was associated with reduced intensive care unit (ICU) and hospitalization times. We found ACE2+ exosomes were induced by SARS-CoV-2 infection and activation of viral sensors in cell culture, which required the autophagy protein ATG16L1, defining these as defensosomes. We further demonstrate that ACE2+

was provided by Faculty Scholar grant from the Howard Hughes Medical Institute (K.C.), Crohn's & Colitis Foundation (K.C.), Kenneth Rainin Foundation (K.C.), Judith & Stewart Colton Center of Autoimmunity (K.C.), NSF Graduate Research Fellowship (K.L.C.), NYU Grossman School of Medicine COVID-19 seed research funds to V.J.T, and a pilot funding from the NYU Langone Health Antimicrobial-resistant Pathogen Program (B.S. and V.J.T.). NYU Langone's Cytometry and Sorting Laboratory, Microscopy Laboratory, Genome Technology Center, and Applied Bioinformatics Laboratory are shared resources partially supported by the Cancer Center Support Grant P30CA016087 at the Laura and Isaac Perlmutter Cancer Center. The funders had no role in the study design, data collection and analysis, decision to publish, or preparation of the manuscript.

Competing interests: I have read the journal's policy and the authors of this manuscript have the following competing interests: K.C. has received research support from Pfizer, Takeda, Pacific Biosciences, Genentech, and Abbvie. K.C. has consulted for or received honoraria from Vedanta, Genentech, and Abbvie. K.C. is an inventor on U.S. patent 10,722,600 and provisional patent 62/935,035 and 63/157,225. V.J.T. receives research support from Janssen Biotech Inc. V.J.T. has consulted for Janssen Research & Development, LLC and have or received honoraria from Genentech and Medimmune. V.J.T. is an inventor on patents and patent applications filed by New York University, which are currently under commercial license to Janssen Biotech Inc. provides research funding and other payments associated with a licensing agreement.

Abbreviations: ALI, air-liquid; BAL, bronchoalveolar lavage; BALF, bronchoalveolar lavage fluid; COVID 19, Coronavirus Disease 2019; gDNA, genomic DNA; HAEC, human airway epithelial culture; HMW, high molecular weight; hpi, hours post infection; ICU, intensive care unit; IFN, interferon; LMW, low molecular weight; MEM, minimal essential medium; MFI, mean fluorescence intensity; NEAA, non-essential amino acid; NP, nucleoprotein; PVDF, polyvinylidene fluoride; RBD, receptor-binding domain; RPM, read per million; RT-PCR, reverse transcriptase polymerase chain reaction; SARS-CoV-2, Severe Acute Respiratory Syndrome Coronavirus 2; TKO, triple knockout; TLR9, toll-like receptor 9.

defensosomes directly bind and block viral entry. These findings suggest that defensosomes may contribute to the antiviral response against SARS-CoV-2 and expand our knowledge on the regulation and effects of extracellular vesicles during infection.

Introduction

Exosomes are a subgroup of single membraned vesicles 40 to 120 nm in diameter secreted by virtually every cell type. Cargo molecules ranging from noncoding RNAs to proteins involved in signal transduction are incorporated during exosome biogenesis, which involves exocytosis of endosomal structures [1]. As such, exosomes mediate intercellular communication events involved in cell proliferation, migration, and cancer [2]. A role in host defense is supported by the finding that exosomes can deliver nucleic acids and other immunogenic moieties from infected cells that elicit interferon (IFN) responses or promote antigen presentation by target cells [3–8]. However, how exosomes are regulated in response to infections remains unclear. A better understanding may inform strategies that seek to use extracellular vesicles as biomarkers or therapeutic agents for infectious disease.

In our previous work, we identified exosomes involved in host defense termed defensosomes that mediated protection against bacterial pore-forming toxins that kill target cells, such as α -toxin produced by *Staphylococcus aureus* [9]. Recognition of bacterial DNA by toll-like receptor 9 (TLR9) led to increased production of defensosomes decorated by ADAM10, the host cell surface target of α -toxin, in a manner dependent on ATG16L1 and other components of the membrane trafficking pathway of autophagy. We further demonstrated that ADAM10⁺ defensosomes serve as decoys that bind α -toxin and prevent cytotoxicity in cell culture and animal models [9]. Therefore, in addition to mediating intercellular communication by transferring signaling molecules between cells, exosomes can also promote host defense through a surface interaction with bacterial proteins. Whether defensosomes are deployed during a viral infection remains unclear.

Severe Acute Respiratory Syndrome Coronavirus 2 (SARS-CoV-2), the respiratory virus responsible for the ongoing global Coronavirus Disease 2019 (COVID-19) pandemic, can cause life-threatening tissue injury to the lung as well as extrapulmonary symptoms that are less understood [10]. Entry into host cells mainly depends on the binding of receptor-binding domain (RBD) of SARS-CoV-2 spike (S) protein to host receptor ACE2. The affinity of SARS-CoV-2 spike for ACE2 is 5 times higher than that of SARS-CoV spike [11] and 1,000 times higher than hemagglutinin of Influenza A for sialic acid [12]. Given this dependence on a high affinity cell surface interaction for viral entry, we hypothesized ACE2-containing defensosomes would inhibit SARS-CoV-2 infection through the binding of the spike protein.

Results

Increased proportion of ACE2+ exosomes in human BAL fluid correlates with reduced time in the ICU

Few studies, if any, have analyzed exosomes in mucosal tissues of patients during an ongoing infection. This is especially true in the setting of SARS-CoV-2 infection where access to lower airway samples were limited due to concerns about possible risks for health care professionals [13–20]. In the airways, ACE2 expression exists as a gradient, with the highest levels in the nasal passageway, down to the lower airways where it is exclusively expressed on type II

pneumocytes [21]. To determine whether ACE2+ exosomes are generated and are present in the respiratory tract, we analyzed bronchoalveolar lavage fluid (BALF) samples from 80 critically ill COVID-19 patients [22] using biochemical fractionation to enrich for exosomes followed by flow cytometry [9]. All patients in our cohort were admitted to the intensive care unit (ICU) due to respiratory failure requiring invasive mechanical ventilation and tested positive for SARS-CoV-2 infection [22]. Applying stringent gating criteria for exosomes, we observed remarkable interindividual variation in the proportion of exosomes with surface ACE2 and the levels of ACE2 present on each exosome measured by mean fluorescence intensity (MFI) (Figs 1A and S1A–S1C). We found that 10 patients had at least 2-fold higher exosome levels in their BALF compared to the mean exosome levels from the other patients. These data suggest that there is variation between individuals in how much ACE2 is loaded into each exosome as well as how many ACE2+ exosomes are produced by each person.

We then asked whether level of ACE2 on exosomes or proportion of ACE2+ exosomes correlate with clinical parameters such as patient age, sex, disease severity, infection status, and other comorbidities linked to SARS-CoV-2 infection such as diabetes or hypertension. Approximately 76.2% of the patients were male, mostly nonwhite (53.8%), with a mean age of 62 years (SD, 14.2). Hypertension and diabetes were reported in 52.5% and 38.3% of patients, respectively (S1 Table). Two patients were excluded from analysis because they were not within 3 standard deviations from the mean (47.96 days) for length of stay in the ICU. As a sensitivity analysis, we also ran the regressions using ACE2 MFI as a predictor of ICU stay outcome, resulting in the same trends in the covariates (S3 Table). Compiling the information regarding the proportion of exosomes that contain ACE2 in patient BALF, we ran different models using clinical data to test whether there was any association with ACE2+ exosomes and length of stay in the ICU, as there was no correlation with mortality. We performed a linear model and a negative binomial model to test this relationship, and we controlled for age, gender, culture results of BAL and blood, diabetes, and hypertension. We also included in a sensitivity analysis model an interaction term between gender, sex, and hypertension, as they are usually correlated. We expressed the coefficients without interactions for simplicity because the estimates did not significantly change. The linear model resulted in negative correlation between length of stay in the ICU and the proportion of ACE2+ exosomes found in the BALF (Table 1, Fig 1B). The negative binomial model predicted similar results (S2 Table). To account for increased length of stay in the ICU due to complications or subsequent infections, we also used ventilation days as an outcome and found that proportion of ACE2+ exosomes remained a significant predictor (S4 and S5 Tables). Also, we did not detect a correlation between ACE2+ exosomes and viral RNA (S1G Fig).

These analyses uncovered a threshold where patients with a proportion of ACE2+ exosomes lower than the mean (38.78%) generally have increased lengths of stay in both the ICU and hospital and increased days on a ventilator (Figs 1 and S1D). Individuals with diabetes (or both diabetes and hypertension) clustered below the average proportion of ACE2+ exosomes (Fig 1C), suggesting common comorbidities may influence the proportion of ACE2+ exosomes. Individuals with hypertension have been shown to have reduced levels of circulating ACE2 with the adverse consequence of increased concentration of the vasoconstricting molecule Angiotensin II due to activation of ACE [23]. However, neither diabetes nor hypertension were associated with statistically significant differences in ACE2 levels on exosomes (S1E and S1F Fig).

Altogether, these data show that the proportion of ACE2+ exosomes and level of ACE2 on individual exosomes in BALF from patients with COVID-19 are highly variable, and their increased presence are associated with a reduction in hospitalization days.

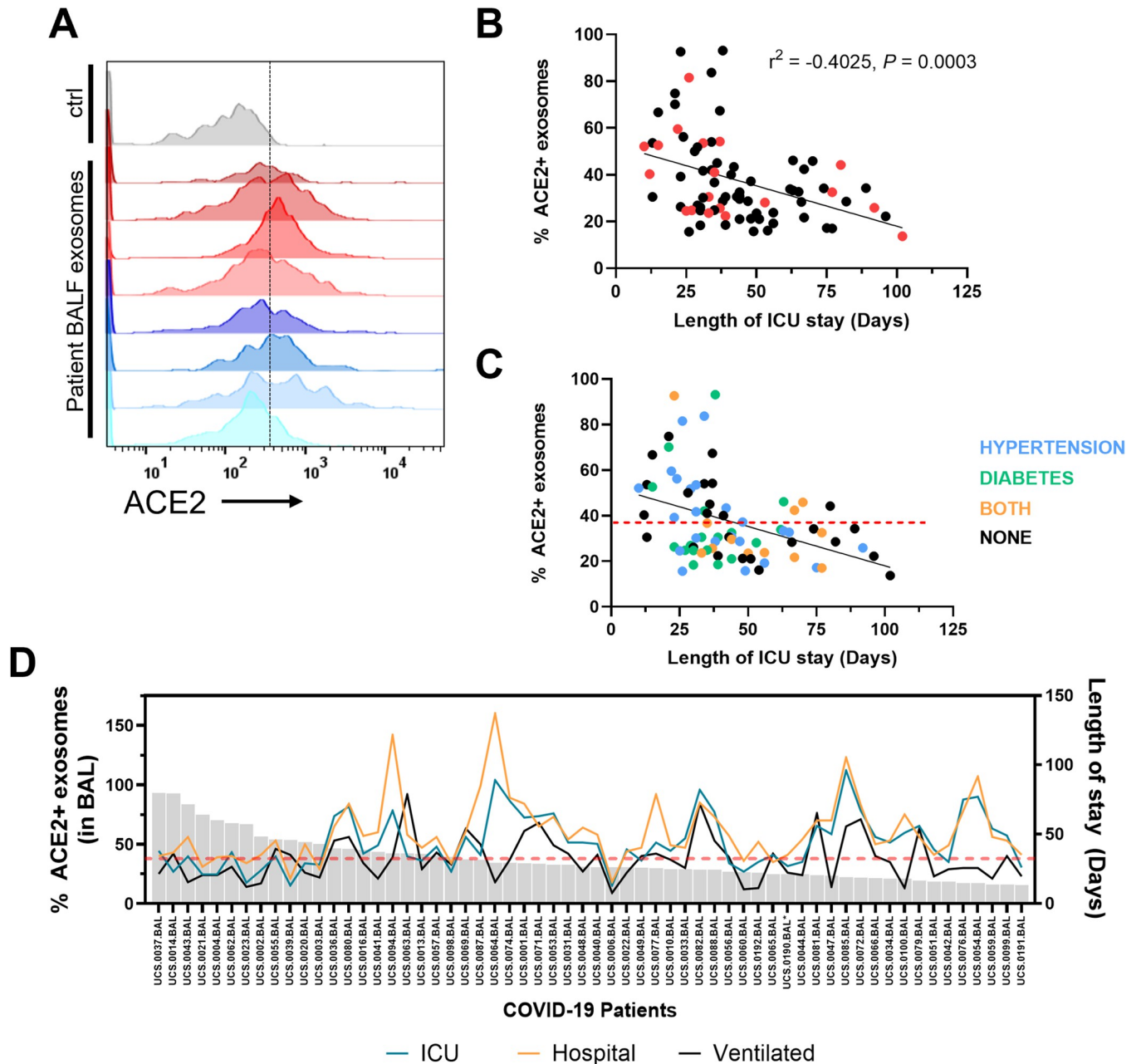


Fig 1. ACE2+ exosomes are associated with reduced length of stay in ICU for COVID-19 patients. (A) Flow cytometry histograms of ACE2 levels on exosomes in BALF from 8 representative COVID-19 patients. Ctrl: isotype control on exosomes from non-covid patient BALF. (B) Correlation analysis of proportion of ACE2+ exosomes in BALF and length of stay in the ICU ($N = 78$). Red dots indicate deaths. Simple regression analysis. (C) Correlation analysis of % ACE2 exosome levels with comorbidities colored: hypertension (blue), diabetes (green), both (orange). Red line indicates the average % of ACE2 + exosomes of all patients. (D) Length of stay in the ICU (blue), total hospitalization time (orange), and time on a ventilator (black) for each COVID patient (excluding deaths) plotted against the proportion of ACE2⁺ exosomes isolated from BALF ($N = 59$). r , Pearson correlation coefficient. P , p -value. Underlying data can be found in [S1 Data](#). BALF, bronchoalveolar lavage fluid; COVID 19, Coronavirus Disease 2019; ICU, intensive care unit.

<https://doi.org/10.1371/journal.pbio.3001754.g001>

Table 1. Predictors of length of stay in the ICU among COVID-19 patients using a linear regression model.

Predictors	Length of stay in ICU (days)		P-Value
	Estimates	CI	
Age (years)	0.2338	-0.5709–1.0385	0.564
% ACE2 positive (BAL exosomes)	-0.549	-0.7845 --0.3136	<0.001
Sex [M]	39.7312	-13.3973–92.8596	0.14
Hypertension	12.1199	-81.5270–105.7668	0.797
BAL <i>C. albicans</i> [Positive]	21.05	6.7861–35.3138	0.004
Blood culture final result [Positive]	5.4402	-3.8165–14.6968	0.245
(Intercept)	50.0676	2.4603–97.6750	0.04
Observations	78		
R2/R2 adjusted	0.375/0.281		

BAL, bronchoalveolar lavage; COVID 19, Coronavirus Disease 2019; ICU, intensive care unit.

<https://doi.org/10.1371/journal.pbio.3001754.t001>

Defensosomes are produced in response to SARS-CoV-2 and antiviral sensors

We previously showed that exosomes are induced by TLR9 activation in response to bacterial DNA or synthetic agonist CpG-A. We found that SARS-CoV-2 infection of A549^{ACE2+} cells also induced robust production of ACE2+ exosomes (Fig 2A). Similar to our observations with bacteria, SARS-CoV-2-induced exosome production was impaired by *ATG16L1* knockdown (Fig 2A). Therefore, the enhanced production of ACE2+ exosomes display a key hallmark of defensosomes—induced in response to an infectious agent in a manner dependent on *ATG16L1*.

Although SARS-CoV-2 is not predicted to directly activate DNA sensors, damage during respiratory tract infection can lead to production of oxidized mitochondrial DNA (ox-mtDNA) [24,25], which is known to be a potent ligand for TLR9 [26]. Stimulation with ox-mtDNA increased exosome production in A549 cells, but this was not observed with sheared genomic DNA (gdDNA) or DNA fragments without any oxidized bases (Fig 2B). We also tested CpG-B, which can activate TLR9, but unlike CpG-A, lacks a phosphodiester backbone and poorly induces IFNs [27]. CpG-B stimulation failed to elicit exosomes from A549 cells (Fig 2C). SARS-CoV-2 has been shown to indirectly activate the cytosolic DNA-sensing pathway dependent on cGAS/STING [28]. However, ligands for cGAS/STING (2'3'-cGAMP and 3'3'-cGAMP) failed to induce exosomes (Fig 2C).

It is possible that IFNs generated downstream of TLR9 activation mediate exosome production. Stimulation of A549 cells with IFN- β induced exosomes in a concentration-dependent manner, where at higher concentrations, the number of exosomes began to decrease (Fig 2D), which may be due to ISGylation and degradation of the compartment where exosomes are generated [29]. IFN- α and IFN- λ 2 also induced exosomes (Fig 2E and 2F). As expected, IFN- β failed to elicit exosomes from triple knockout (TKO) A549 cells that lack receptors necessary for recognition of all 3 major classes of IFNs (IFNAR, IFNGR, and IFNLR) (Fig 2G). In contrast, TKO A549 cells were still able to produce exosomes in response to CpG-A (Fig 2H). Thus, IFN stimulation is sufficient to induce exosome production, but are not required downstream of nucleic acid sensing.

SARS-CoV-2 infection generates viral ssRNA and dsRNA that may serve as signals to induce exosomes. When transfected into cells, low and high molecular weight versions of the dsRNA mimetic poly I:C preferentially activate the cytosolic RNA sensors RIG-I and MDA-5,

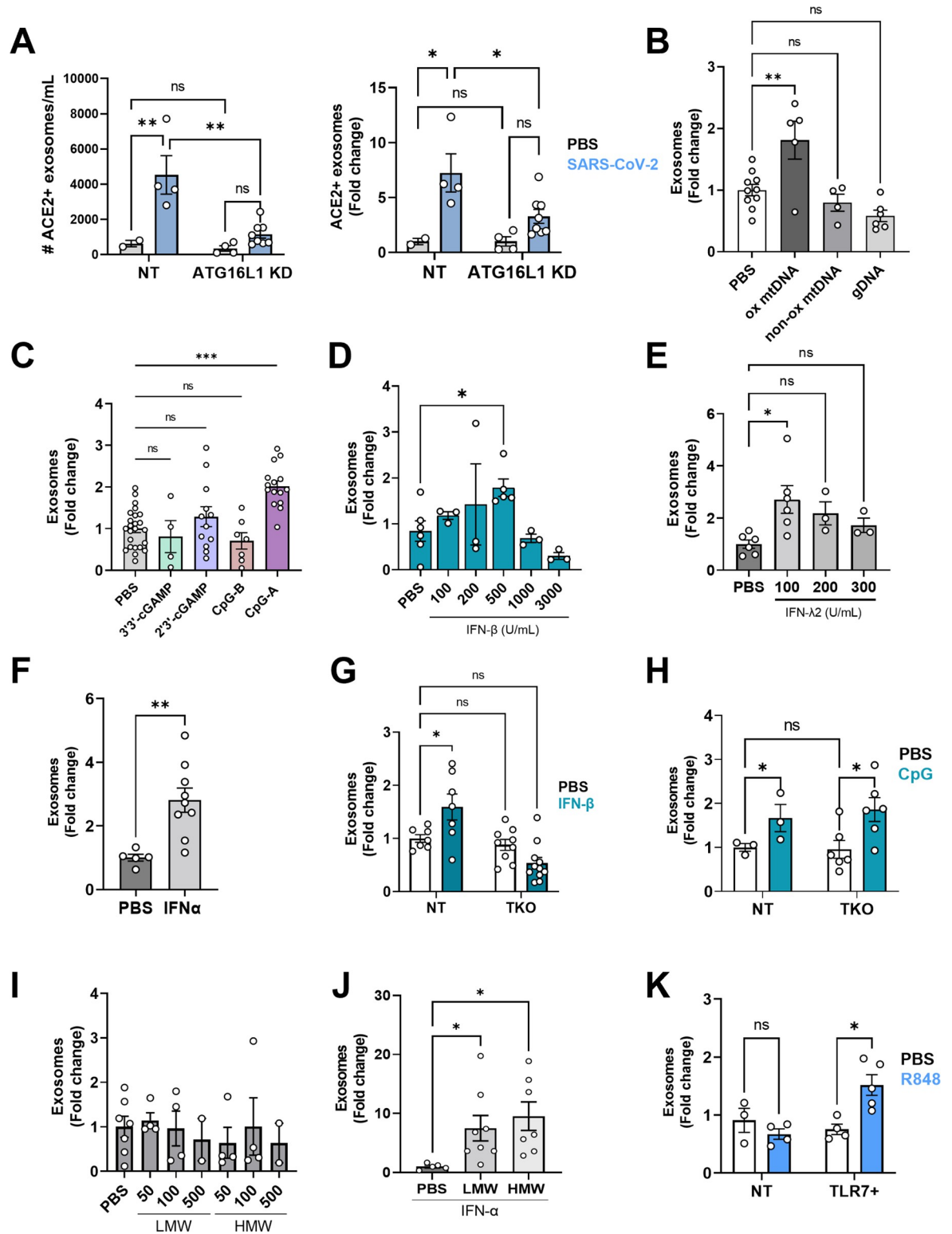


Fig 2. TLR ligands and SARS-CoV-2 induce exosome production. (A) ACE2⁺ A549 (NT) and ACE2⁺ A549 cells knocked down for ATG16L1 using shRNA (ATG16L1 KD) were infected with TCID50 SARS-CoV-2 USA-WA1/2020 for 72 h. Exosomes were isolated from supernatants and quantified in exact counts (left) and fold change (right). (B) Quantification of exosomes from A549 cell-culture supernatant by flow cytometry 16 h after stimulation with 32 μg of oxidized mtDNA (ox mtDNA), mtDNA products without oxidized bases (non-ox mtDNA), or genomic DNA (gDNA) (*n* = 4–10). (C) Quantification of exosomes from A549 cells stimulated for 16 h with

1 $\mu\text{g}/\text{mL}$ 3'3'-cGAMP ($n = 4$), 2'3'-cGAMP ($n = 9$), 0.5 μM CpG-A ($n = 8$), and 0.5 μM CpG-B ($n = 7$). CpG-A will be referred to as CpG from this point on. (D) Quantification of exosomes from A549 cells stimulated with various dilutions of IFN- β for 16 h ($n = 3-6$). (E) Quantification of exosomes from A549 cells stimulated with various dilutions of IFN- λ for 16 h ($n = 3-6$). (F) Quantification of exosomes following stimulation of A549 cells with 100 U/mL IFN- β for 16 h ($n = 5-9$). (G) Exosome quantification of IFNAR/ γ R/ λ R TKO A549 cells stimulated with 500 U/mL IFN- β for 16 h compared to non-transduced (NT) A549 cells ($n = 7-11$). (H) Quantification of exosomes from NT A549 or TKO A549 cells stimulated with CpG for 16 h ($n = 3-6$). (I) Quantification of exosomes from A549 cells stimulated with HMW or LMW Poly I:C with LyoVec at 50, 100, 500 ng/mL ($n = 2-7$). (J) Exosomes were quantified from A549 cells pretreated with 100 U/mL IFN α for 24 h, followed by stimulation with 10 $\mu\text{g}/\text{mL}$ LMW or HMW PolyI:C. (K) Quantification of exosomes from A549 cells and TLR7-expressing A549 cells stimulated with 1 $\mu\text{g}/\text{mL}$ R848 for 16 h ($n = 3-5$). (A-K): Exosomes: CD9+ CD63+ CD81+ events. Measurements were taken from distinct samples. Error bars represent mean \pm SEM and at least 2 independent experiments were performed. Underlying data can be found in [S1 Data](#). C-F, I, J One-way ANOVA with multiple comparisons with Dunnett's post-test. A, G, H, K Two-way ANOVA using Dunnett's post-test. * $P \leq 0.05$; ** $P \leq 0.01$. HMW, high molecular weight; LMW, low molecular weight; ns, not significant; NT, non-transduced; SARS-CoV-2, Severe Acute Respiratory Syndrome Coronavirus 2; TKO, triple knockout.

<https://doi.org/10.1371/journal.pbio.3001754.g002>

respectively, but we found that neither induced exosomes (Fig 2I). In A549 cells, the endosomal dsRNA sensor TLR3 is expressed at low levels; IFN- α treatment induces TLR3 to functionally active levels, allowing A549 cells to become sensitive to untransfected poly I:C [30]. Following pretreatment with IFN α for 24 h, A549 cells produced 10- to 20-fold more exosomes in response to poly I:C without a transfection agent (Fig 2J). A549 cells do not express the endosomal ssRNA sensors TLR7 or TLR8. We found that ectopic expression of TLR7 led to exosome induction upon stimulation with a synthetic agonist, R848 (Fig 2K). Therefore, multiple innate immune ligands associated with SARS-CoV-2 infection and IFNs induce exosome production.

An IFN-inducible splice variant of ACE2 (dACE2) missing the N-terminal region necessary for SARS-CoV-2 binding has been identified [31–33]. Using an antibody targeting the C-terminus of ACE2 (Abcam 15348), we readily detected full-length ACE2, but not dACE2 protein in exosomes induced by bafilomycin or IFN α in various cell lines using western blotting (S6 Fig), consistent with reports indicating that dACE2 is post-transcriptionally unstable [32]. We found that the antibody used for the flow cytometry experiments (R&D AF933) exclusively detected full-length ACE2. Hence, we can conclude that full-length ACE2 is incorporated into exosomes from BALF. With available RNA-seq data on the cellular fraction of BALF from our patient cohort [22], we were able to detect low expression of dACE2 in 50 out of 80 patients (S4A Fig). dACE2 expression did not correlate with disease severity (length of ICU stay), but positively correlated with the proportion of ACE2+ exosomes and ACE2 MFI on exosomes found in the BAL (S4B–S4D Fig). dACE2 expression only negatively correlated with 2 genes previously identified to have a positive correlation with dACE2 from data on bronchial tumors in the TCGA-LUSC database (S5A–S5T Fig) [33]. As dACE2 lacks the catalytic component of full-length ACE2 and the binding site for Spike and is expressed at low levels, we believe dACE2 has no direct impact on exosome neutralization of SARS-CoV-2, but may be a reflection of IFN responses.

Given that IFNs induce exosome production (Fig 2D–2F), we next asked whether ACE2+ exosome production was linked to the IFN response in our cohort of patients. We performed differential gene analysis on “high” ACE2+ exosome producers or individuals with “high” ACE2 levels on their exosomes compared to their “low” counterparts. We found that “high” ACE2+ exosome producers had an enrichment of genes found in the Coronavirus pathogenesis pathway and activation of cytosolic PRRs, and a down-regulation of pathways related to EIF2 signaling and oxidative phosphorylation. ACE2 MFI “high” individuals had an enrichment in IFN and PI3K/AKT signaling pathways (S7–S9 Figs). These findings reinforce the association between antiviral signaling and defensosome production.

ACE2+ defensosomes neutralize SARS-CoV-2 virions

Our finding that ACE2+ exosomes in patient BALF display an inverse correlation with length of hospital stay raised the possibility that they play a role during viral infection akin to our previous description of defensosomes during bacterial toxinosis. Therefore, we tested whether addition of exosomes can protect Vero E6 cells, which are highly susceptible to SARS-CoV-2 infection (Fig 3A). Exosomes were isolated from A549^{ACE2+} cells (Fig 3B) and mixed with human SARS-CoV-2 USA WA1/2020 isolate at an MOI of 0.01. We included a polyclonal neutralizing antibody targeting spike (nAb) as a positive control. Addition of ACE2+ exosomes led to a dose-dependent reduction in viral nucleoprotein (NP) staining by immunofluorescence microscopy at 24 h post-infection (Figs 3C and 3D and S2A), whereas ACE2- exosomes from untransduced control A549s failed to inhibit infection. Also, addition of the microvesicle fraction that does not contain exosomes (5,000xg) did not decrease infection levels (Fig 3C). We also tested neutralization in human airway epithelial cultures (HAECs), an air-liquid interfact (ALI) model that contains all major cell types found in the bronchial epithelium (basal, ciliated, secretory), organized in pseudostratified architecture [34]. Addition of ACE2+ exosomes mixed with SARS-CoV-2 to the apical side (“lumen”) blocked infection of HAECs, while ACE2- exosomes did not show any significant effect (Figs 3E and S2B).

We next tested whether inducing exosome production protects against viral infection without the need of adding exogenous exosomes from donor cells. We found that pretreatment with CpG-A, which we confirmed induces exosome production by Vero E6 cells in a manner dependent on ATG16L1 (Fig 3F and 3G), led to a reduction in cells infected with SARS-CoV-2 (Fig 3H). Removing the exosome-containing supernatant prior to infection led to similar levels of SARS-CoV-2 infection as unstimulated cells (Figs 3H and S2C). Further, knockdown of *ATG16L1* in either A549 cells or Vero E6 cells did not impact viral replication levels in either cell type (S2D and S2E Fig). Vero E6 cells generally cannot produce IFNs [35,36], although hantavirus infection was shown to elicit IFN λ from these cells [37]. To formally demonstrate that the exosome fraction of the supernatant from CpG-A-treated Vero E6 cells contains the antiviral activity, we biochemically isolated exosomes and tested whether they inhibit SARS-CoV-2 infection of target cells. The enriched exosomes were sufficient to reduce viral infection, and the degree of inhibition was even greater than the unmanipulated supernatant. Together, these results show that defensosomes can inhibit SARS-CoV-2 infection.

ACE2+ defensosomes directly interact with SARS-CoV-2

We next used electron microscopy techniques to visualize the interactions between SARS-CoV-2 virions and defensosomes. Viral particles with predicted spherical shape and uniform size of 80 to 100 nm in diameter were detected by negative stain imaging in control suspensions containing SARS-CoV-2 virions alone (Fig 4A) [38]. With the addition of exosomes, we detected structures with the characteristic collapsed morphology of exosomes clustered around particles with virion morphology. The difficulty in distinguishing exosomes and virions due to their similar shape and size precluded quantification of the data. Therefore, we used immunogold labeling in which exosomes and SARS-CoV-2 virions were identified by an anti-CD63 antibody coupled to 18-nm gold particle and an anti-NP antibody coupled to a nanogold particle (1.4 nm), respectively (Fig 4B). We observed an enrichment of CD63 labeling around SARS-CoV-2 virions when incubated with ACE2+ exosomes, but not ACE2- exosomes (Fig 4C). The pronounced clustering of CD63 in the ACE2+ exosome-virus mixtures may be indicative of multiple exosomes bound to the virions (or vice versa); however, we cannot definitively conclude the number of exosomes due to the lack of contrast of the exosome membranes.

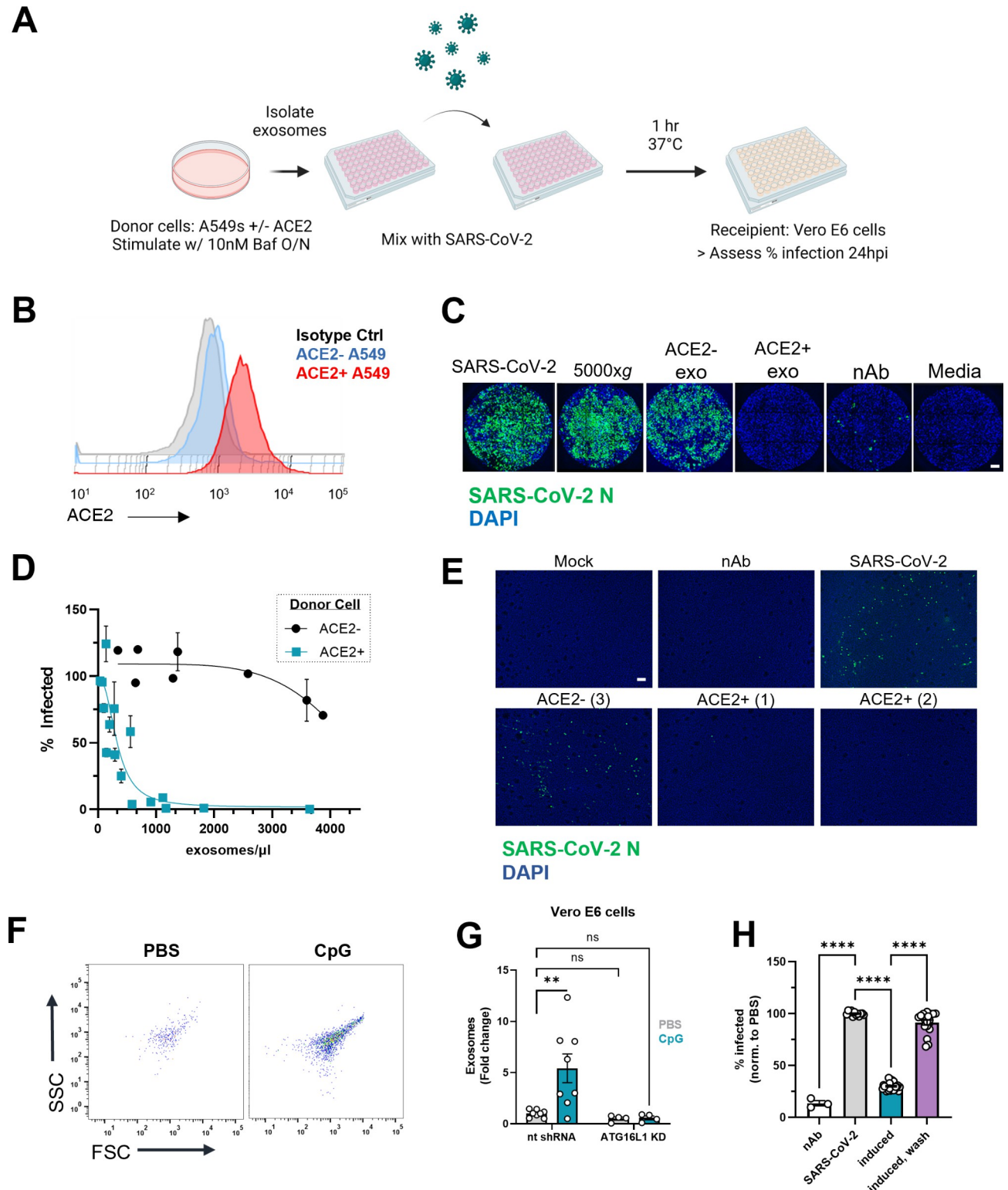


Fig 3. ACE2+ exosomes protect against SARS-CoV-2 infection. (A) Workflow for exosome neutralization assay used to assess protective effects of mixing SARS-CoV-2 and exosomes. Created with BioRender.com. (B) Representative histogram of cell-surface ACE2 on A549 and A549^{ACE2} cells. (C) Representative immunofluorescence images of Vero E6 cells infected with SARS-CoV-2, pellet from 5,000xg spin, approximately 20 K exosomes from ACE2⁻ cells, approximately 20 K exosomes from ACE2⁺ cells, neutralizing antibody, or with media alone stained for viral N protein. Scale bar: 0.625 mm. (D) Percentage of infected Vero E6 cells based on positive staining for N protein after infection with SARS-CoV-2 mixed with exosomes isolated

from A549^{ACE2} (teal) or untransduced A549 cells (black). Compiled means \pm SEM from 5 experiments, values normalized to infection with SARS-CoV-2 alone. (E) Representative immunofluorescence images of HAECs infected with mock (media only control), SARS-CoV-2 alone, approximately 11 K (1) or approximately 22 K (2) ACE2+ exosomes with virus, approximately 150 K (3) ACE2- exosomes with virus, and neutralizing antibody with virus (nAb). Images were taken 72 hpi. Scale bar: 0.156 mm. (F) Representative flow cytometry plots of exosomes isolated from Vero E6 cells stimulated with CpG. FSC: forward scatter, SSC: side scatter. (G) Quantification of exosomes from Vero E6 cells and Vero E6 cells transduced with a non-targeting shRNA for ATG16L1 stimulated with PBS ($n = 4$) or 1 μ M CpG-A ($n = 4$) for 16 h. (H) Quantification of infected cells after infection of Vero E6 cells with SARS-CoV-2 only, SARS-CoV-2 mixed with supernatants of cells pretreated overnight with CpG-A (induced), or SARS-CoV-2 added to CpG-A pretreated cells following removal of supernatant (wash). Exosomes: CD9, CD63, CD81+, PKH67+ events. Means \pm SEM of at least 2 independent experiments. G Two-way ANOVA with Dunnett's post-test compared to NT PBS. H One-way ANOVA with Dunnett's post-test compared to PBS. Error bars represent the mean \pm SEM of at least 2 independent experiments, with measurements taken from distinct samples. Underlying data can be found in [S1 Data](#). ** $P \leq 0.01$; **** $P \leq 0.0001$. HAEC, human airway epithelial culture; hpi, hours post infection; ns, not significant; SARS-CoV-2, Severe Acute Respiratory Syndrome Coronavirus 2.

<https://doi.org/10.1371/journal.pbio.3001754.g003>

Lastly, we applied cryo-electron microscopy and tomography to confirm these associations between SARS-CoV-2 virions and ACE2+ exosomes. Virions were easily distinguished by the presence of protrusions that resembled the club-like head of the spike protein and exosomes were larger single-membraned vesicles, spherical or ellipsoid in shape. Focusing on the area between the viral and exosome membranes, we were able to visualize an elongated structure resembling the post-fusion form of spike and ACE2 in some tomograms ([S3A and S3B Fig](#), [S2 Data](#) and [S3 Data](#)). Tomographic reconstruction also captured several virions around larger exosomes as well as potential virions inside an exosome ([S4 Data](#)). Collectively, these data demonstrate that the presence of ACE2 on exosomes increases binding and clustering of virions.

Discussion

Our analyses of an inpatient cohort of COVID-19 patients revealed ACE2 levels on exosomes in BALF can display striking interindividual variability, and that a high proportion of ACE2+ exosomes, especially those with increased surface levels, are associated with reduced hospital stay. A limitation of these analyses is that BALF was only collected from subjects experiencing severe disease. Although it is unclear whether ACE2+ exosomes are a marker or have a causative role in recovery from SARS-CoV-2 infection, our cell culture experiments indicate that they can inhibit viral infection by serving as defensosomes. The ability to produce sufficient numbers of defensosomes is key to providing optimal protection in vitro, and thus, understanding the factors that contribute to variable exosome production at mucosal surfaces during SARS-CoV-2 infection and other conditions will be of great interest. Transcriptional regulation and cleavage by proteases such as ADAM10 and ADAM17 [39] may also explain heterogeneity in ACE2+ exosomes. Other unanswered questions include how ACE2+ exosome release affects the availability of ACE2 in the tissue and whether this impacts acute injury to the lung, another function of this critical enzyme involved in cardiovascular processes [40]. Also, we focused on surface protein interactions, but it is important to consider other ways SARS-CoV-2 infection can be impacted by exosomes, which have been shown to facilitate the transfer of viral and cellular components to target cells with either pro-viral or antiviral consequences depending on the pathogen [41–43].

Infection by SARS-CoV-2 and other coronaviruses leads to formation of structures resembling autophagosomes [44–46], double-membrane vesicles generated during autophagy that target intracellular material to the lysosome for degradation [47]. Several SARS-CoV-2 proteins inhibit formation of autophagosomes or prevent the acidification of lysosomes and endosomes, promoting viral egress from the cell [48–53]. Although viruses such as SARS-CoV-2 evade autophagy-mediated degradation during intracellular replication, our results suggest extracellular virions may be subject to neutralization by defensosomes generated through an

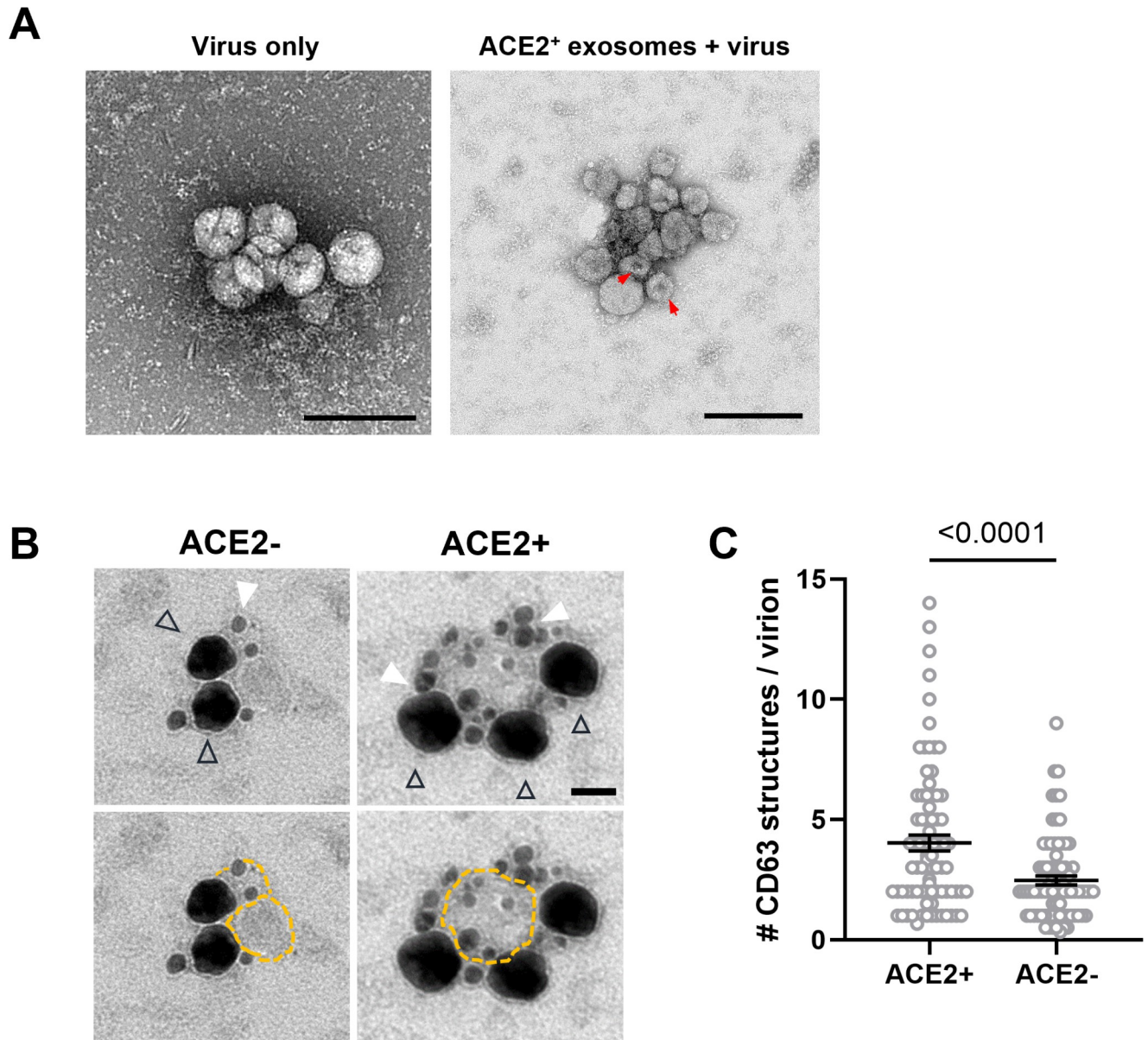


Fig 4. SARS-CoV-2 virions associate with ACE2⁺ exosomes. (A) TEM of negative stained exosomes and virus alone. Arrowheads: putative exosomes. Scale bars: 200 nm. Red arrows mark the characteristic collapsing of exosomes during TEM imaging. (B) Double immunogold labeling TEM images of SARS-CoV-2 virions mixed with ACE2⁺ exosomes (right panel, scale bar: 50 nm) or ACE2⁻ exosomes (left panel). Virions are labeled using an antibody for SARS-CoV-2 N, followed by nanogold-conjugated Fab (black triangle outline), which fills the entirety of the virion giving it the appearance of the larger dark mass. Exosomes are labeled using an antibody against CD63, followed by 18-nm colloidal gold-conjugated IgG (filled white triangles). Bottom panels are the same images as the top panels, with exosome membranes marked with dotted yellow outlines denotes to enhance their visibility. (C) Quantification of CD63 structures per virion present in a cluster containing both markers. ACE2⁺ ($n = 68$ clusters), ACE2⁻ ($n = 57$). Error bars represent mean \pm SEM from at least 2 independent experiments. Underlying data can be found in [S1 Data](#). Unpaired t test with Welch's correction. * $P \leq 0.05$; ** $P \leq 0.01$; *** $P \leq 0.001$; **** $P \leq 0.0001$. ns, not significant; SARS-CoV-2, Severe Acute Respiratory Syndrome Coronavirus 2; TEM, transmission electron microscopy.

<https://doi.org/10.1371/journal.pbio.3001754.g004>

autophagy-like process dependent on ATG16L1. In this context, it is notable that defensosomes are induced by innate immune activation of TLRs that require a signaling endosome [54,55], which may coincide with the location from which exosomes are generated. The termination of TLR7 signaling is mediated by the packaging of TLR7 into exosomes via an ESCRT independent mechanism involving ALIX and the recruitment of syntenin-1 by UNC93B1

[56], providing precedence for coupling viral RNA recognition with extracellular vesicle trafficking. Cells that produce significant amounts of IFN in response to sensing of viral PAMPs through TLRs, such as plasmacytoid dendritic cells [57], could play an important role in initiating early protection by activating cells in distal tissues to release exosomes.

The finding that innate immune pathways induce exosomes raises the possibility that defensosomes represent a broader antiviral defense strategy. High affinity virus–host receptor pairings, like SARS-CoV-2 Spike and ACE2, could determine whether a given virus is vulnerable to neutralization. In the case of lower affinity interactions where direct neutralization may not occur, defensosomes may be playing secondary roles in the transfer of antiviral molecules to surrounding cells such as IFITM proteins [58,59]. A better understanding of which cargos are selectively loaded into exosomes could help predict situations in which defensosomes impact viral pathogenesis.

Several clinical trials are underway for exosome-based therapies against various cancers and kidney disease [60–62]. The advantage of strategies involving exosomes includes their scalability, stability in biofluids, and ability to be engineered to carry desired receptors and even deliver drugs. Our results support a broad innate antimicrobial function for defensosomes that includes defense against viral disease. An improved understanding of defensosome regulation may inform clinical applications.

Materials and methods

Cohort of critically ill COVID-19 patients

The characteristics of this cohort have recently been described [22]. Briefly, we enrolled adults (>18 years old) admitted to the ICU due to respiratory failure requiring invasive mechanical ventilation with confirmed diagnosis of SARS-CoV-2 infection by reverse transcriptase polymerase chain reaction (RT-PCR). Lower airway samples (bronchoalveolar lavage (BAL)) were obtained during clinically indicated bronchoscopy performed for airway clearance or for percutaneous tracheostomy placement. Surviving subjects signed informed consent to participate in this study while samples and metadata from subjects who died or were incapacitated were de-identified and included in this study. All patients or their legal representative agreed to participate via our NYU IRB approved protocol (IRB no. s16-00122/01598). The study protocol was approved by the Institutional Review Board of New York University.

Cell culture and lentivirus production

A549 cells were purchased from ATCC. A549^{ACE2} cells were generated using lentiviral transduction of a human ACE2 cDNA-expressing plasmid (backbone: pLV-EF1a-IRES-Puro (Addgene 85132)) as previously described [34]. TLR7+ A549 were generated by lentiviral transduction of pcDNA3-TLR7-YFP (a gift from Doug Golenbock (Addgene plasmid # 13022; <http://n2t.net/addgene:13022>; RRID:Addgene_13022)). A549^{ACE2} cells were selected using 1 µg/mL puromycin. Cells were cultured with 10% Dulbecco's modified Eagle medium (DMEM (Gibco), 10% fetal calf serum (FCS), 1% non-essential amino acids (NEAA), 1% Penicillin/Streptomycin) and filtered using a 0.22 µm filter unit (Millipore). Vero E6 cells were purchased from ATCC (cat. No. CLR-1586) and maintained in same media as A549 cells, but including 10 mg/mL Amphotericin B. 293FTs were maintained in same media as A549 cells. Lentivirus was produced by transfecting 10-cm plate of 293FTs with 10 µg of plasmid using Lipofectamine 3000. Media was exchanged the next day and lentivirus was collected the following day; 1 mL lentivirus was used to transduce A549 cells using Polybrene (Millipore). TKO (IFNAR1/IFNLR/IFNGR1) A549 cells were generously provided by Marco Binder at the German Cancer Research Center (DKFZ), Heidelberg, Germany [63].

Stimulations were done with 0.5 μ M CpG-ODN 2216 (Class A) or CpG-ODN 2006 (Class B) (Invivogen), 1 μ g/mL R848 (Invivogen), human IFN- β (R&D), IFN- λ 2 (cat. No. 8417-IL-025, R&D), IFN α (cat. No 11200-2, R&D), 1 μ g/mL 3'3'-cGAMP, 1 μ g/mL 2'3'-cGAMP (Invivogen), PolyI:C LMW and HMW with and without LyoVec (Invivogen), and Bafilomycin A1 (Sigma-Aldrich, B1793). Calu-3 cells were cultured in DMEM with 10% FCS, 1% HEPES, 1% NEAAs, and 1% Pen-Strep.

BSL3

Plaque and neutralization assays were performed in the BSL3 facility of NYU Grossman School of Medicine, in accordance with its Biosafety Manual and Standard Operating Procedures.

Plaque assay

Viral titers were determined by plaque assay. Vero E6 cells were seeded into 12-well plates to reach confluency the next day. When confluent, cells were washed twice with PBS (Ca/Mg+) before the infection with 1:10 serial dilutions of the samples for 1 h at 37°C. At 1 h post virus addition, virus was removed, cells were washed again twice with PBS (Ca/Mg+), and overlay-medium was added (minimal essential medium (MEM), 1.5 μ g/mL Trypsin-TPCK, 1.6% Oxoid-Agar, 1% Pen-Strep, 1% GlutaMax, 20 mM HEPES, 0.4% BSA, and 0.24% NaHCO₃). At 72 h post infection, the cells were fixed by adding 10% formalin solution for 24 h. After fixation, overlay was removed and cells were stained with crystal violet solution (0.1% crystal violet in 1.9% ethanol and 19% methanol in cell culture grade H₂O) for at least 30 min. Plates were rinsed once with H₂O before determining the viral titer.

Virus amplification

All SARS-CoV-2 stock preparations and subsequent infection assays were performed in the CDC/USDA-approved biosafety level 3 (BSL-3) facility in compliance with NYU Grossman School of Medicine guidelines for BSL-3. SARS-CoV-2 isolate USA-WA1/2020, deposited by the Centers for Disease Control and Prevention, was obtained through BEI Resources, NIAID, NIH (cat. no. NR-52281; GenBank accession number MT233526). The USA-WA1/2020 stock was passaged twice in Vero E6 cells to generate a passage 6 working stock (1.0E+06 PFU/mL) for our studies.

In vitro neutralization assay

The 3.2×10^4 Vero E6 cells were seeded in black 96-flat well with clear bottom plates 24 h before infection. SARS-CoV-2 was mixed 1:1 v/v with exosomes in infection media (DMEM, 10% HEPES, 10% NEAA) and allowed to bind for 1 h at 37°C. Heat-inactivated plasma (56°C for 1 h) from a convalescent patient was used as a positive control. Confluent Vero cells were then infected with this exosome-virus mixture. At 24 hours post infection (hpi), plates were fixed with 10% formalin solution for 30 to 45 min and then washed with dH₂O. Plates were permeabilized with 0.1% Triton-X 100, blocked with 1% BSA/PBS, and stained for SARS-CoV-2 N mouse monoclonal SARS-CoV-2 anti-N antibody 1C7 (1:1,000, kind gift of Thomas Moran) overnight at 4°C. Plates were then incubated with Alexa Fluor 647 goat anti-mouse Ab (1:2,000) and DAPI (1:2,000) at 37°C for 1 h. After 3 washes with PBS, plates were imaged using the Cell Insight CX7 LZR high-content screening platform. Images were analyzed and quantified with HCS Navigator software.

Infection and immunofluorescence of HAECs

Maintenance of HAECs were done as described in [34]. At 48 h prior to infection, 6- to 8-week-old HAECs were washed apically twice for 30 min each with prewarmed PBS (Ca/Mg +). At 1 h prior to infection, cultures were washed apically twice for 30 min each with prewarmed PBS. Each culture was infected with a viral dilution containing with $1.35E+05$ PFU with or without exosomes for 2 h at 37°C. The inoculum was removed, and the cultures were washed 3 times with prewarmed PBS. For each washing step, PBS was added to the apical surface, and cultures were incubated at 37°C for 30 min before the PBS was removed. The third wash was collected and stored at -80°C for titration by plaque assay on Vero E6 cells. Infectious particles were collected every 24 h (up to 72 h) by adding 60 µl of prewarmed PBS, incubating at 37°C for 30 min, and washes were stored at -80°C. Wells were fixed by submerging in 10% formalin for 24 h and washed 3 times with PBS before analysis by immunofluorescence. Fixed HAECs were quenched 50 mM NH₄Cl (in PBS), permeabilized using a solution of, 0.1% Saponin, and blocked with 2% BSA. Cultures were stained with anti-SARS nucleocapsid protein antibody that cross reacts with SARS-CoV-2 N (1:1,000, cat. no. 200-401-A50; Rockland) and goat-anti-rabbit Alexa Fluor 488 and DAPI.

Mitochondrial DNA generation

Short mitochondrial DNA fragments (221 bp) were amplified from gDNA from A549 cells with and without 8-Oxo-2'-deoxyguanosine-5'-Triphosphate (TriLink Biotechnologies) using GoTaq Mastermix. Forward primer: 5'-CCCCACAAACCCCATTAACCCCA-3'. Reverse: 5'-TTTCATCATGCGGAGATGTTGGATGG-3'. Fragments were isolated using Quick PCR Clean Up kit (Qiagen). Genomic DNA fragments were generated by sonicating genomic DNA isolated from A549 cells (Qiagen Blood and Tissue DNeasy kit) using genomic DNA tips (20 g).

shRNA knockdown

Lentivirus based knockdown of human *ATG16L1* (5'-ACTGTAGCTTTGCCGTGAATG-3') was performed using MISSION shRNA constructs (Sigma-Aldrich) and psPAX2 packaging system. psPAX2 was a gift from Didier Trono (Addgene plasmid # 12260). Lentivirus-expressing shRNAs were produced by DNA transfection using Lipofectamine 3000 (Thermo Fisher). Transduction was performed using Polybrene (Millipore) and selection was done using 1 µg/mL puromycin.

Flow cytometry

Exosomes pellets were stained with 100 µl of an antibody cocktail in 1× PBS (Corning) containing anti-CD9 (human HI9a, mouse MZ3), anti-CD63 (human H5C6, mouse NVG-2), anti-CD81 antibodies (human 5a6, mouse Eat-2) from Biolegend, and anti-human ACE2 (R&D Biosystems cat no. FABAF9332R) at 1:100 for 1 h at 4°C, rocking. Exosomes were stained with PKH67 cell linker dye (Sigma). Exosomes were washed with 1× PBS once and ultracentrifuged at 100,000xg for 1.5 h. The exosome pellet was resuspended in PBS. Cells and exosomes were analyzed using a Beckman Coulter Cytoflex S cytometer at the slowest flow rate.

Exosome isolation

Cell culture supernatants were spun at 500xg for 10 min, followed by a 10,000xg spin for 10 min. Supernatants were passed through a 0.22 µm filter (Millex-GP PES). Supernatants were

washed with 1× PBS and pelleted by ultracentrifugation at 100,000×g for 1.5 h. Exosomes used for neutralization were resuspended in viral media (10% DMEM, 1% HEPES, 1% PenStrep) and transferred to a non-TC round bottom 96-well plate (Corning).

All human BAL samples were processed into cellular and supernatant fractions before freezing for further analysis. Exosomes were isolated from 200 μ l of thawed acellular BAL fluid and fixed to a final concentration of 4% PFA before being removed from the BSL-3 facility. Samples were washed with PBS and ultracentrifuged at 100,000×g for 1.5 h before staining for flow cytometry analysis.

Western blotting

The 1×10^6 cells were collected, washed once with PBS, and lysed using RIPA buffer containing 10× protease inhibitor cocktail (Roche). Lysates were centrifuged at 20,000g for 20 min at 4°C. Samples were reduced using 4× SDS sample loading buffer and 10× reducing buffer, and then boiled at 95°C for 3 min. Exosomes isolated by differential centrifugation were resuspended directly in sample loading buffer and boiled. Protein was run at 120 V for 1 h using a 2% to 12% gradient protein gel (Thermo Fisher Scientific). Proteins were transferred to an Immuno-Blot polyvinylidene fluoride (PVDF) membrane using Bio-Rad wet transfer apparatus for 1 h at 120 V. Membranes were blocked with LICOR blocking buffer for 1 h and incubated with mouse anti- β -actin (Sigma) at 1:1,000, polyclonal goat anti-ACE2 (R&D AF933) at 1:1,000, polyclonal rabbit anti-ACE2 at 1:1,000 (Abcam, cat# ab15348), monoclonal mouse anti-CD63 (Abcam, cat# ab217345), or monoclonal mouse anti-CD9 (R&D, cat# MAB25292) at 1:1,000 overnight at 4°C. Membranes were washed 3 times for 5 min with PBS-T and probed with donkey anti-rabbit LICOR IRdye 800CW, donkey anti-goat 680RD, goat anti-mouse 800CW, or goat anti-rabbit LICOR IRdye 800CW/680RD (LICOR Biosciences) for 1 h at RT. Membranes were imaged on a LICOR Odyssey CLX imaging system.

Negative stain, immunogold labeling, and cryo-electron tomography

Exosomes isolated from A549 and A549^{ACE2} cells stimulated with Bafilomycin A1 were mixed with SARS-CoV-2 and allowed to bind for 1 h at 37°C in the BSL3 before being fixed with 4% PFA. Suspensions of SARS-CoV-2/exosomes were ultracentrifuged once at 100,000 \times g to pellet and then resuspended in PBS before processing for TEM imaging.

Negative stain of exosome-virus mixtures involved deposit of 3 μ l of 4% paraformaldehyde fixed exosomes on glow discharged carbon copper grids. Grids were stained with 1% uranyl acetate and were imaged under FEI Talos L120C TEM and photographed with a Gatan (4k \times 4k) OneView camera (Gatan, Pleasanton, California, United States of America).

For double immunogold labeling, exosome-virus mixtures in PBS were fixed to final concentration of 4% PFA and placed on glow-discharged formvar-carbon copper grids for 20 min. Staining was done as follows: Grids were washed with PBS (pH 7.4) twice for 2 min each followed by incubation with PBS/glycine 50 mM for 3 min. Grids were permeabilized and blocked with 0.1% Saponin/1% cold-water fish skin gelatin (Perm buffer) for 10 min and first stained with anti-human CD63 (Abcam, ab59479) antibody (1:10) in Perm buffer for 1.5 h. Grids were washed 6× with PBS with 0.1% Saponin for 2 min and then incubated with 18-nm gold-conjugated anti-mouse antibody (18-nm colloidal gold AffiniPure goat anti-mouse IgG (H+L), Jackson ImmunoResearch Laboratories, West Grove, Pennsylvania, USA), in Perm buffer for 30 min. After washing with PBS, grids were fixed in 2% PFA in PBS for 5 min.

Grids were washed with PBS and then incubated in PBS/50 mM glycine for 3 min to quench the unbounded aldehyde group. The grids were incubated with anti-NP antibody (1:100) in perm buffer for 1.5 h followed by anti-mouse Fab nanogold (1:250, Nanoprobe,

New York, USA) in perm buffer for 30 min. Grids were fixed in 1% glutaraldehyde in PBS for 5 min, washed with distilled water, followed by washes with 0.02 M sodium citrate buffer (pH 7.0). The silver enhancement is done using HQ Silver enhancement kit (#2012, HQ Silver, Nanoprobe, New York, USA) for 9 min and rinsed with ddH₂O. Finally, grids were contrasted with 3% uranyl acetate and embedded with 2% methylcellulose in a ratio of 1 to 9.

Immunogold and nanogold double labeling was quantified using ImageJ software (NIH).

CryoEM sample collection

Samples for CryoET were plunge frozen in liquid ethane with a VitroBot Mark IV (Thermo Fisher) at 20°C at 100% humidity on C-flat (Protochips, Morrisville, North Carolina, USA) 1.2/1.3 grids with 80 s easyGlow (Ted Pella, Redding, California, USA) glow discharge. All images were acquired on the Talos Arctica (Thermo Fisher) housed at NYU. Images were taken at 200 kV with a Gatan K3 imaging system (Gatan, Pleasanton, California, USA) collected at 28,000× nominal magnification. The calibrated super-resolution pixel size of 0.7040 Å was used for processing.

Micrographs were collected using Legion [64,65] at a dose rate of 11.21 e⁻/Å²/s with a total exposure of 3.50 s, for an accumulated dose of 39.23 e⁻/Å². Intermediate frames were recorded every 0.07 s for a total of 50 frames per micrograph. Frames were aligned using Motioncor2 [66].

Tilt series were collected using SerialEM [67] at a dose rate of 11.21 e⁻/Å²/s with a total exposure of 0.25 s for an accumulated dose of 2.79 e⁻/Å² per tilted image. Intermediate frames were recorded every 0.05 s for a total of 5 frames per micrograph. Movies were collected in super-resolution mode. Tilt series were acquired in a bidirectional pattern starting from -18°, with a range from -60° to 60° in 3° step with a total dose of 114e⁻/Å².

Tilt series processing

Frames were aligned using Warp [68], binned to the physical pixel size of 1.408 Å, and constructed into a tilt series stack for further processing. Micrographs within each tilt series were aligned with EMAN2 [69] and constructed into a tomogram at binning 4 (5.63 Å/pixel) using Fourier inversion. Tomograms were denoised using Topaz [70]. Denoised tomograms were inspected using IMOD [71] and clipped to appropriate size. Movies were made from selected tomograms using ImageJ. Automated segmentation was performed using EMAN2 to segment membranes, and further 3D rendering and refinement of Spike proteins was done manually on ORS Dragonfly (Object Research Systems, Quebec, Canada).

Patient correlation analysis

Anonymized data contained patient demographics, medications prescribed during hospital admission, vitals upon entry to the hospital, reported comorbidities, spike and RBD antibody titers, and blood and lung culture results. All analyses were performed in R Studio (version 1.4.1717).

RNA-seq analysis for dACE2 transcripts

Raw reads can be found using Bioproject accession: PRJNA688510. Sequencing reads were mapped to the reference genome (hg38) using the STAR aligner (v2.5.0c) [72]. Alignments were guided by a Gene Transfer Format (GTF) file. The mean read insert sizes and their standard deviations were calculated using Picard tools (v.1.126) (<http://broadinstitute.github.io/picard>). The read count tables were generated using HTSeq (v0.6.0) [73], normalized based on

their library size factors using DEseq2 [74], and differential expression analysis was performed. transcript per million (TPM) values for transcript abundances were calculated using kallisto (v. 0.46.2) [75]. The read per million (RPM) normalized BigWig files were generated using BEDTools (v2.17.0) [76] and bedGraphToBigWig tool (v4). Gene set enrichment analysis was performed using GSEA tool (PMID: 16199517). To compare the level of similarity among the samples and their replicates, we used 2 methods: principal-component analysis and Euclidean distance-based sample clustering. All the downstream statistical analyses and generating plots were performed in R environment (v3.1.1) (<https://www.r-project.org/>). The pathway analyses and signaling networks for S8 and S9 Figs were generated through the use of QIAGEN IPA (QIAGEN, <https://digitalinsights.qiagen.com/IPA>) [77].

Statistical analyses

Statistical analyses were performed using GraphPad Prism 9.0 (GraphPad Software, San Diego, California, USA; <https://www.graphpad.com/>). All graphs show the mean and standard error of the mean (SEM). An unpaired 2-tailed *t* test was used to evaluate differences between 2 groups with Welch's correction. One-way ANOVA with Dunnett's post-test was used to evaluate experiments involving groups of 3 or more. Two-way ANOVA with Dunnett's or Šidák's post-test was used to evaluate groups with more than one variable. Correlation was analyzed using Pearson *r*. For each test, a *p*-value <0.05 is considered statistically significant. Clinical data was analyzed using R-studio. We performed descriptive analysis extracting data from EHR for these patients and summarizing this data with R. Linear model was used with the outcome as length of stay in the ICU. As a sensitivity analysis, we also performed a negative binomial model, with ACE2 MFI as a predictor instead of % ACE2 positivity, which yielded the same results.

Supporting information

S1 Data. Excel spreadsheet containing, in separate sheets, the underlying numerical data for Figs 1A–1D, 2A–2K, 3B, 3D, 3G, 3H, 4C, S1B–S1G, S2A, S2B, S2C, S2E, S2F, S4A–S4D, S5A–S5T and S7.

(XLSX)

S2 Data. Tomograms from Cryo-ET of SARS-CoV-2 and ACE2⁺ exosomes. Scanning through all frames (forward and backward) of selected tomogram in S3A Fig. Generated in ImageJ.

(MP4)

S3 Data. Rotational video of S4B Fig. Each grid is a 10 nm square.

(MP4)

S4 Data. Additional video of tomographic reconstructions of exosomes and virions.

(MP4)

S1 Raw images. Raw Western blot images for S6 Fig.

(PDF)

S1 Fig. Characteristics of exosomes from COVID-19 patient BALF. (A) Gating strategy and representative flow cytometry plots from patient BALF. Exosomes were stained for antibodies against CD63, CD9, CD81, and ACE2. Exosomes were labeled with a lipid-intercalating dye, PKH67. FSC: forward scatter. SSC: side scatter. (B) Surface ACE2 on exosomes isolated from acellular BALF measured by MFI using flow cytometry. (C) Percentage of ACE2⁺ exosomes out of total exosomes in A. (D) Correlation between percentage of ACE2⁺ exosomes and

length of stay in the ICU (orange line) and hospital (teal line) for all patients (including deaths) ($N = 80$). ACE2 levels on exosomes stratified by positive or negative patient status for (E) diabetes and (F) hypertension ($N = 80$). (G) Correlation between viral RNA copies and percent ACE2+ exosomes ($N = 80$). Red dotted lines indicate the average ACE2 MFI on ACE2+ exosomes in B or the average proportion of ACE2+ exosomes in C calculated from all COVID patients. Error bars show mean \pm SEM. Underlying data can be found in [S1 Data](#). E, F Unpaired Mann–Whitney t test. G Simple linear regression. * $P \leq 0.05$; ** $P \leq 0.01$; *** $P \leq 0.001$; **** $P \leq 0.0001$. BALF, bronchoalveolar lavage fluid; COVID 19, Coronavirus Disease 2019; ICU, intensive care unit; MFI, mean fluorescence intensity; ns, not significant. (TIFF)

S2 Fig. Characterizing role of exosomes against SARS-CoV-2 in vitro. (A) Infection level in [Fig 3D](#) against number of donor A549^{ACE2+} or A549 cells (in 15 cm plates). (B) Number of infectious particles measured by plaque assay from apical washes every 24 h for 72 h of HAECs infected with SARS-CoV-2 alone (red), SARS-CoV-2 and ACE2+ exosomes (blue), SARS-CoV-2 and ACE2- exosomes (green), and SARS-CoV-2 with neutralizing Ab (gray); # corresponds to number of input plates (15 cm). (C) Representative immunofluorescence images of Vero E6 cells infected with SARS-CoV-2 where the cells were stimulated/pretreated with PBS, CpG, or nAb from [Fig 3F](#). Scale bar: 1.25 mm. (D) Infection level 24 hpi with SARS-CoV-2 of *ATG16L1* KD or non-targeting shRNA control (NT) A549^{ACE2+} cells. (E) Infection level 24 hpi with SARS-CoV-2 in *ATG16L1* KD or NT control Vero E6 cells. Virus dilution in (D) and (E) corresponds to the step in a 2-fold dilution series of SARS-CoV-2 (MOI: 0.01). (F) Infection level of Vero E6 cells following infection with media alone, SARS-CoV-2 alone, or SARS-CoV-2 mixed with supernatant from Vero E6 cells stimulated with CpG-A or enriched exosomes from CpG-A stimulated Vero E6 cells. Error bars show mean \pm SEM, with measurements taken from distinct samples. Underlying data can be found in [S1 Data](#). F One-way ANOVA with Dunnett's post-test compared to SARS-CoV-2. **** $P \leq 0.0001$. HAEC, human airway epithelial culture; hpi, hours post infection; KD, knockdown; ns, not significant; SARS-CoV-2, Severe Acute Respiratory Syndrome Coronavirus 2. (TIFF)

S3 Fig. Cryo-EM tomogram and 3D rendering of an exosome and SARS-CoV-2 virion. (A) Representative tomographic slice of a SARS-CoV-2 virion and an exosome. Exosomes were isolated from ACE2+ A549 cells. Inset white arrow: spike, scale bar: 50 nm. (B) Three-dimensional model of 1 individual exosome (gray) and SARS-CoV-2 virion with a membrane (green) and spike proteins (red) generated from segmentation. Scale bar: 10 nm. SARS-CoV-2, Severe Acute Respiratory Syndrome Coronavirus 2. (TIFF)

S4 Fig. Low expression of the short ACE2 isoform dACE2 detected in a subset of COVID patients. (A). Normalized expression of dACE2 measured by RNA-seq (TPM) from the cellular fraction of BAL fluid isolated from hospitalized COVID patients ($N = 70$). (B). dACE2 expression correlated against ACE2 MFI (C) % ACE2+ exosomes and (D) length of stay in the ICU ($N = 70$). Underlying data can be found in [S1 Data](#). ** $P \leq 0.01$; **** $P \leq 0.0001$. ICU, intensive care unit; MFI, mean fluorescence intensity; ns, not significant; SARS-CoV-2, Severe Acute Respiratory Syndrome Coronavirus 2; TPM, transcript per million. (TIFF)

S5 Fig. Correlation of dACE2 expression in COVID patients with various ISGs. (A–T) Correlation analysis of dACE2 and HLA-E (A), TAP1 (B), TRIM21 (C), RTP4 (D), IRF9 (E), UBE2L6 (F), B2M (G), CXCL10 (H), IFI27 (I), IFIT3 (J), HERC6 (K), DTX3L (L), WARS1

(M), IL1RN (N), STAT1 (O), IFI44L (P), OAS2 (Q), GBP1 (R), (S), and MX1 (T) expression in the cellular fraction of BAL fluid from COVID patients. Samples were excluded if transcriptome mapping was lower than 60% ($N = 67$). Simple linear regression was performed for A–T. Each data point represents a patient. * $P \leq 0.05$; ** $P \leq 0.01$; *** $P \leq 0.001$; **** $P \leq 0.0001$. ns, not significant; TPM, transcript per million.

(TIFF)

S6 Fig. Full-length ACE2 and not dACE2 is loaded onto exosomes. (A) Representative western blots of exosomes from A549 cells expressing full-length ACE2 (ACE2+ A549), dACE2 expressing A549 cells (dACE2+ A549), Calu3 cells, and untransduced A549 cells after stimulation with bafilomycin A1 (B) or IFN- α (I) using 2 different anti-ACE2 antibodies, R&D AF933 (above) and Abcam 15348 (below). R&D AF933 was used for flow cytometry experiments and recognizes full-length ACE2 but not dACE2. Abcam 15348 was raised against the C-terminal region of ACE2 and recognizes both isoforms. Cell lysate from unstimulated HAECs was used as a control for detection of dACE2 protein. dACE2 was not detected in exosome fractions, even when supernatants were from cells ectopically expressing this isoform (dACE2+ A549). Asterisk denotes nonspecific band. HAEC, human airway epithelial culture.

(TIFF)

S7 Fig. Heatmap of IPA analysis including comparisons between “high” and “low” groups for %ACE2+ exosomes and ACE2 MFI value. “High” and “low” groups were designated based on whether the measured values of %ACE2+ exosomes and ACE2 MFI for an individual patient were above or below the mean computed value across all patients for each variable. Percent: % ACE2+ exosomes. Red and blue indicate up-regulated and down-regulated pathways in the “high” group for each variable, respectively. IPA, Ingenuity Pathway Analysis; MFI, mean fluorescence intensity.

(TIFF)

S8 Fig. Signaling pathway analysis of differentially expressed genes in the “high” %ACE2 + exosome group. Generated using IPA. IPA, Ingenuity Pathway Analysis.

(TIFF)

S9 Fig. Signaling pathway analysis of differentially expressed genes in the “high” ACE2 MFI exosome group. Generated using IPA. IPA, Ingenuity Pathway Analysis; MFI, mean fluorescence intensity.

(TIFF)

S1 Table. Demographics and clinical characteristics of the COVID-19 patient cohort. Summary of hospitalized COVID-19 patients from which the ACE2+ exosomes were measured from the BALF. Data expressed as n (%) or median [IQR]. BMI, body mass index. BMI is the weight in kilograms divided by the square of the height in meters. CHF: congestive heart failure; CAD: coronary artery disease; CKD: chronic kidney disease; CVA: cerebrovascular accident. HLD: hyperlipidemia; HTN: Hypertension; ECMO: extracorporeal membrane oxygenation. Respiratory culture: defined as having any respiratory culture performed. Positive bacteria: a culture resulting in any bacterial growth. Blood culture: defined as having any blood culture performed. ICU: intensive care unit; Ventilator days: total number of days on mechanical ventilation.

(PDF)

S2 Table. Regression using negative binomial model and length of stay in the ICU as the outcome. p, P -value, CI, confidence interval.

(PDF)

S3 Table. Linear regression on covariates including ACE2 MFI using length of stay in the ICU as the outcome. p, *P*-value, CI, confidence interval.

(PDF)

S4 Table. Linear regression on covariates including ACE2 MFI using ventilation days as an outcome. p, *P*-value, CI, confidence interval.

(PDF)

S5 Table. Regression using negative binomial model and ventilation days as the outcome. p, *P*-value, CI, confidence interval.

(PDF)

Acknowledgments

We thank the Office of Science & Research High-Containment Laboratories at NYU Grossman School of Medicine for their support in the completion of this research and the NYU Langone Health's Microscopy Laboratory and CryoEM Core. We also thank Marco Binder's group for providing the TKO A549 cells, Rachel Prescott for maintaining HAECs, and Kamal Khanna, Stephen T. Yeung, Ralf Duerr, and Yonghua Li for handling the processing of BALF samples. Fig 2A was created using BioRender, terms of use found at <https://biorender.com/academic-license/>. We would like to thank the Genome Technology Center (GTC) for expert library preparation and sequencing and the Applied Bioinformatics Laboratories (ABL) for providing bioinformatics support and Jun-Chieh J. Tsay for helping with the analysis and interpretation of the data. This work has used computing resources at the NYU School of Medicine High Performance Computing (HPC) Facility.

Author Contributions

Conceptualization: Krystal L. Ching, Meike Dittmann, Victor J. Torres, Ken Cadwell.

Data curation: Krystal L. Ching, Clea Barnett, Alireza Khodadadi-Jamayran, Leopoldo N. Segal.

Formal analysis: Krystal L. Ching, Maren de Vries, Juan Gago, Kristen Dancel-Manning, Joseph Sall, William J. Rice, Clea Barnett, Alireza Khodadadi-Jamayran, Feng-Xia Liang, Bo Shopsin.

Funding acquisition: Victor J. Torres, Ken Cadwell.

Investigation: Krystal L. Ching, Maren de Vries, Juan Gago, Victor J. Torres, Ken Cadwell.

Methodology: Maren de Vries, Kristen Dancel-Manning, Joseph Sall, William J. Rice, Feng-Xia Liang, Leopoldo N. Segal.

Resources: Alireza Khodadadi-Jamayran, Aristotelis Tsirigos.

Supervision: Aristotelis Tsirigos, Lorna E. Thorpe, Bo Shopsin, Leopoldo N. Segal, Meike Dittmann, Victor J. Torres, Ken Cadwell.

Validation: Maren de Vries, Alireza Khodadadi-Jamayran.

Visualization: Maren de Vries.

Writing – original draft: Krystal L. Ching, Victor J. Torres, Ken Cadwell.

Writing – review & editing: Krystal L. Ching, Maren de Vries, Juan Gago, Kristen Dancel-Manning, Joseph Sall, William J. Rice, Clea Barnett, Feng-Xia Liang, Lorna E. Thorpe, Bo Shopsin, Leopoldo N. Segal, Meike Dittmann, Victor J. Torres, Ken Cadwell.

References

1. Mathieu M, Martin-Jaular L, Lavieu G, They C. Specificities of secretion and uptake of exosomes and other extracellular vesicles for cell-to-cell communication. *Nat Cell Biol.* 2019; 21(1):9–17. Epub 2019/01/04. <https://doi.org/10.1038/s41556-018-0250-9> PMID: 30602770.
2. Kalluri R, LeBleu VS. The biology, function, and biomedical applications of exosomes. *Science.* 2020; 367(6478).
3. Cheng Y, Schorey JS. Extracellular vesicles deliver Mycobacterium RNA to promote host immunity and bacterial killing. *EMBO Rep.* 2019; 20(3):e46613. <https://doi.org/10.15252/embr.201846613> PMID: 30683680
4. Nandakumar R, Tschismarov R, Meissner F, Prabakaran T, Krissanaprasit A, Farahani E, et al. Intracellular bacteria engage a STING–TBK1–MVB12b pathway to enable paracrine cGAS–STING signaling. *Nat Microbiol.* 2019; 4(4):701–713. <https://doi.org/10.1038/s41564-019-0367-z> PMID: 30804548
5. Sisquella X, Ofir-Birin Y, Pimentel MA, Cheng L, Abou Karam P, Sampaio NG, et al. Malaria parasite DNA-harboring vesicles activate cytosolic immune sensors. *Nat Commun.* 2017; 8(1):1–15.
6. Smith VL, Cheng Y, Bryant BR, Schorey JS. Exosomes function in antigen presentation during an in vivo Mycobacterium tuberculosis infection. *Sci Rep.* 2017; 7(1):1–12.
7. Utsugi-Kobukai S, Fujimaki H, Hotta C, Nakazawa M, Minami M. MHC class I-mediated exogenous antigen presentation by exosomes secreted from immature and mature bone marrow derived dendritic cells. *Immunol Lett.* 2003; 89(2–3):125–131. [https://doi.org/10.1016/s0165-2478\(03\)00128-7](https://doi.org/10.1016/s0165-2478(03)00128-7) PMID: 14556969
8. Hui WW, Emerson LE, Clapp B, Sheppe AE, Sharma J, Del Castillo J, et al. Antigen-encapsulating host extracellular vesicles derived from Salmonella-infected cells stimulate pathogen-specific Th1-type responses in vivo. *PLoS Pathog.* 2021; 17(5):e1009465. <https://doi.org/10.1371/journal.ppat.1009465> PMID: 33956909
9. Keller MD, Ching KL, Liang FX, Dhabaria A, Tam K, Ueberheide BM, et al. Decoy exosomes provide protection against bacterial toxins. *Nature.* 2020; 579(7798):260–4. Epub 2020/03/07. <https://doi.org/10.1038/s41586-020-2066-6> PMID: 32132711; PubMed Central PMCID: PMC7519780.
10. Wu T, Zuo Z, Kang S, Jiang L, Luo X, Xia Z, et al. Multi-organ Dysfunction in Patients with COVID-19: A Systematic Review and Meta-analysis. *Aging Dis.* 2020; 11(4):874–94. Epub 2020/08/09. <https://doi.org/10.14336/AD.2020.0520> PMID: 32765952; PubMed Central PMCID: PMC7390520.
11. Walls AC, Park Y-J, Tortorici MA, Wall A, McGuire AT, Veesler D. Structure, function, and antigenicity of the SARS-CoV-2 spike glycoprotein. *Cell.* 2020; 181(2):281–92. e6. <https://doi.org/10.1016/j.cell.2020.02.058> PMID: 32155444
12. Xiong X, Coombs PJ, Martin SR, Liu J, Xiao H, McCauley JW, et al. Receptor binding by a ferret-transmissible H5 avian influenza virus. *Nature.* 2013; 497(7449):392–6. Epub 2013/04/26. <https://doi.org/10.1038/nature12144> PMID: 23615615.
13. Chen L, Liu W, Zhang Q, Xu K, Ye G, Wu W, et al. RNA based mNGS approach identifies a novel human coronavirus from two individual pneumonia cases in 2019 Wuhan outbreak. *Emerg Microbes Infect.* 2020; 9(1):313–9. Epub 2020/02/06. <https://doi.org/10.1080/22221751.2020.1725399> PMID: 32020836; PubMed Central PMCID: PMC7033720.
14. Harrison L, Ramsden J, Winter S, Rocke J, Heward E. Tracheostomy guidance during the COVID-19 Pandemic. *ENT UK.* 2020. Epub 2020/03/19.
15. McGrath BA, Brenner MJ, Warrillow SJ, Pandian V, Arora A, Cameron TS, et al. Tracheostomy in the COVID-19 era: global and multidisciplinary guidance. *Lancet Respir Med.* 2020; 8(7):717–25. Epub 2020/05/19. [https://doi.org/10.1016/S2213-2600\(20\)30230-7](https://doi.org/10.1016/S2213-2600(20)30230-7) PMID: 32422180; PubMed Central PMCID: PMC7228735.
16. Michetti CP, Burlew CC, Bulger EM, Davis KA, Spain DA, Critical C, et al. Performing tracheostomy during the Covid-19 pandemic: guidance and recommendations from the Critical Care and Acute Care Surgery Committees of the American Association for the Surgery of Trauma. *Trauma Surg Acute Care Open.* 2020; 5(1):e000482. Epub 2020/05/06. <https://doi.org/10.1136/tsaco-2020-000482> PMID: 32368620; PubMed Central PMCID: PMC7186881.
17. Parker NP, Schiff BA, Fritz MA, Rapoport SK, Schild S, Altman KW, et al. Tracheostomy recommendations during the COVID-19 pandemic. *American Association of Otolaryngology-Head and Neck Surgery.* 2020.

18. Shen Z, Xiao Y, Kang L, Ma W, Shi L, Zhang L, et al. Genomic diversity of severe acute respiratory syndrome–coronavirus 2 in patients with coronavirus disease 2019. *Clin Infect Dis*. 2020; 71(15):713–720. <https://doi.org/10.1093/cid/ciaa203> PMID: 32129843
19. Shiba T, Ghazizadeh S, Chhetri D, St John M, Long J. Tracheostomy Considerations during the COVID-19 Pandemic. *OTO Open*. 2020; 4(2):2473974X20922528. Epub 2020/04/29. <https://doi.org/10.1177/2473974X20922528> PMID: 32342026; PubMed Central PMCID: PMC7175063.
20. Sommer DD, Engels PT, Weitzel EK, Khalili S, Corsten M, Tewfik MA, et al. Recommendations from the CSO-HNS taskforce on performance of tracheotomy during the COVID-19 pandemic. *J Otolaryngol Head Neck Surg*. 2020; 49(1):23. Epub 2020/04/29. <https://doi.org/10.1186/s40463-020-00414-9> PMID: 32340627; PubMed Central PMCID: PMC7184547.
21. Hou YJ, Okuda K, Edwards CE, Martinez DR, Asakura T, Dinnon KH III, et al. SARS-CoV-2 reverse genetics reveals a variable infection gradient in the respiratory tract. *Cell*. 2020; 182(2):429–46. e14. <https://doi.org/10.1016/j.cell.2020.05.042> PMID: 32526206
22. Sulaiman I, Chung M, Angel L, Koralov S, Wu B, Yeung ST, et al. Microbial signatures in the lower airways of mechanically ventilated COVID19 patients associated with poor clinical outcome. *Nat Microbiol*. 2021; 6:1245–1258. <https://doi.org/10.1038/s41564-021-00961-5> PMID: 34465900
23. Oudit GY, Crackower MA, Backx PH, Penninger JM. The role of ACE2 in cardiovascular physiology. *Trends Cardiovasc Med*. 2003; 13(3):93–101. Epub 2003/04/15. [https://doi.org/10.1016/s1050-1738\(02\)00233-5](https://doi.org/10.1016/s1050-1738(02)00233-5) PMID: 12691672.
24. Scozzi D, Cano M, Ma L, Zhou D, Zhu JH, O'Halloran JA, et al. Circulating mitochondrial DNA is an early indicator of severe illness and mortality from COVID-19. *JCI Insight*. 2021; 6(4). <https://doi.org/10.1172/jci.insight.143299> PMID: 33444289
25. Shenoy S. Coronavirus (Covid-19) sepsis: revisiting mitochondrial dysfunction in pathogenesis, aging, inflammation, and mortality. *Inflamm Res*. 2020; 69(11):1077–85. Epub 2020/08/09. <https://doi.org/10.1007/s00011-020-01389-z> PMID: 32767095; PubMed Central PMCID: PMC7410962.
26. Caielli S, Athale S, Domic B, Murat E, Chandra M, Banchereau R, et al. Oxidized mitochondrial nucleoids released by neutrophils drive type I interferon production in human lupus. *J Exp Med*. 2016; 213(5):697–713. Epub 2016/04/20. <https://doi.org/10.1084/jem.20151876> PMID: 27091841; PubMed Central PMCID: PMC4854735.
27. Kerkmann M, Rothenfusser S, Hornung V, Towarowski A, Wagner M, Sarris A, et al. Activation with CpG-A and CpG-B oligonucleotides reveals two distinct regulatory pathways of type I IFN synthesis in human plasmacytoid dendritic cells. *J Immunol*. 2003; 170(9):4465–4474. <https://doi.org/10.4049/jimmunol.170.9.4465> PMID: 12707322
28. Neufeldt CJ, Cerikan B, Cortese M, Frankish J, Lee J-Y, Plociennikowska A, et al. SARS-CoV-2 infection induces a pro-inflammatory cytokine response through cGAS-STING and NF- κ B. *Commun Biol*. 2022; 5(1):1–15.
29. Villarroya-Beltri C, Baixauli F, Mittelbrunn M, Fernandez-Delgado I, Torralba D, Moreno-Gonzalo O, et al. ISGylation controls exosome secretion by promoting lysosomal degradation of MVB proteins. *Nat Commun*. 2016; 7(1):13588. Epub 2016/11/25. <https://doi.org/10.1038/ncomms13588> PMID: 27882925; PubMed Central PMCID: PMC5123068.
30. Tissari J, Siren J, Meri S, Julkunen I, Matikainen S. IFN- α enhances TLR3-mediated antiviral cytokine expression in human endothelial and epithelial cells by up-regulating TLR3 expression. *J Immunol*. 2005; 174(7):4289–94. Epub 2005/03/22. <https://doi.org/10.4049/jimmunol.174.7.4289> PMID: 15778392.
31. Blume C, Jackson CL, Spalluto CM, Legebeke J, Nazlamova L, Conforti F, et al. A novel ACE2 isoform is expressed in human respiratory epithelia and is upregulated in response to interferons and RNA respiratory virus infection. *Nat Genet*. 2021; 53(2):205–214. <https://doi.org/10.1038/s41588-020-00759-x> PMID: 33432184
32. Ng KW, Attig J, Bolland W, Young GR, Major J, Wrobel AG, et al. Tissue-specific and interferon-inducible expression of nonfunctional ACE2 through endogenous retroelement co-option. *Nat Genet*. 2020; 52(12):1294–1302. <https://doi.org/10.1038/s41588-020-00732-8> PMID: 33077915
33. Onabajo OO, Banday AR, Stanifer ML, Yan W, Obajemu A, Santer DM, et al. Interferons and viruses induce a novel truncated ACE2 isoform and not the full-length SARS-CoV-2 receptor. *Nat Genet*. 2020; 52(12):1283–1293. <https://doi.org/10.1038/s41588-020-00731-9> PMID: 33077916
34. de Vries M, Mohamed AS, Prescott RA, Valero-Jimenez AM, Desvignes L, O'Connor R, et al. A comparative analysis of SARS-CoV-2 antivirals characterizes 3CLpro inhibitor PF-00835231 as a potential new treatment for COVID-19. *J Virol*. 2021; 95(10):e01819–e01820.
35. Desmyter J, Melnick JL, Rawls WE. Defectiveness of interferon production and of rubella virus interference in a line of African green monkey kidney cells (Vero). *J Virol*. 1968; 2(10):955–61. Epub 1968/10/

01. <https://doi.org/10.1128/JVI.2.10.955-961.1968> PMID: 4302013; PubMed Central PMCID: PMC375423.
36. Mosca JD, Pitha PM. Transcriptional and posttranscriptional regulation of exogenous human beta interferon gene in simian cells defective in interferon synthesis. *Mol Cell Biol.* 1986; 6(6):2279–83. Epub 1986/06/01. <https://doi.org/10.1128/mcb.6.6.2279-2283.1986> PMID: 3785197; PubMed Central PMCID: PMC367773.
37. Prescott J, Hall P, Acuna-Retamar M, Ye C, Wathelet MG, Ebihara H, et al. New World hantaviruses activate IFN λ production in type I IFN-deficient vero E6 cells. *PLoS ONE.* 2010; 5(6):e11159. Epub 2010/06/23. <https://doi.org/10.1371/journal.pone.0011159> PMID: 20567522; PubMed Central PMCID: PMC2887373.
38. Ke Z, Oton J, Qu K, Cortese M, Zila V, McKeane L, et al. Structures and distributions of SARS-CoV-2 spike proteins on intact virions. *Nature.* 2020; 588(7838):498–502. Epub 2020/08/18. <https://doi.org/10.1038/s41586-020-2665-2> PMID: 32805734; PubMed Central PMCID: PMC7116492.
39. Jia HP, Look DC, Tan P, Shi L, Hickey M, Gakhar L, et al. Ectodomain shedding of angiotensin converting enzyme 2 in human airway epithelia. *Am J Physiol Lung Cell Mol Physiol.* 2009; 297(1):L84–L96. <https://doi.org/10.1152/ajplung.00071.2009> PMID: 19411314
40. Imai Y, Kuba K, Rao S, Huan Y, Guo F, Guan B, et al. Angiotensin-converting enzyme 2 protects from severe acute lung failure. *Nature.* 2005; 436(7047):112–116. <https://doi.org/10.1038/nature03712> PMID: 16001071
41. Hassanpour M, Rezaie J, Nouri M, Panahi Y. The role of extracellular vesicles in COVID-19 virus infection. *Infect Genet Evol.* 2020; 85:104422. Epub 2020/06/17. <https://doi.org/10.1016/j.meegid.2020.104422> PMID: 32544615; PubMed Central PMCID: PMC7293471.
42. Kalamvoki M, Du T, Roizman B. Cells infected with herpes simplex virus 1 export to uninfected cells exosomes containing STING, viral mRNAs, and microRNAs. *Proc Natl Acad Sci U S A.* 2014; 111(46):E4991–6. Epub 2014/11/05. <https://doi.org/10.1073/pnas.1419338111> PMID: 25368198; PubMed Central PMCID: PMC4246290.
43. Saha B, Kodys K, Adejumo A, Szabo G. Circulating and exosome-packaged hepatitis C single-stranded RNA induce monocyte differentiation via TLR7/8 to polarized macrophages and fibrocytes. *J Immunol.* 2017; 198(5):1974–1984. <https://doi.org/10.4049/jimmunol.1600797> PMID: 28122964
44. Klein S, Cortese M, Winter SL, Wachsmuth-Melm M, Neufeldt CJ, Cerikan B, et al. SARS-CoV-2 structure and replication characterized by in situ cryo-electron tomography. *Nat Commun.* 2020; 11(1):1–10.
45. Reggiori F, Monastyrska I, Verheije MH, Cali T, Ulasli M, Bianchi S, et al. Coronaviruses Hijack the LC3-I-positive EDEMosomes, ER-derived vesicles exporting short-lived ERAD regulators, for replication. *Cell Host Microbe.* 2010; 7(6):500–508. <https://doi.org/10.1016/j.chom.2010.05.013> PMID: 20542253
46. Prentice E, Jerome WG, Yoshimori T, Mizushima N, Denison MR. Coronavirus replication complex formation utilizes components of cellular autophagy. *J Biol Chem.* 2004; 279(11):10136–10141. <https://doi.org/10.1074/jbc.M306124200> PMID: 14699140
47. Klionsky DJ, Petroni G, Amaravadi RK, Baehrecke EH, Ballabio A, Boya P, et al. Autophagy in major human diseases. *EMBO.* 2021; 40(19):e108863. <https://doi.org/10.15252/embo.2021108863> PMID: 34459017
48. Ghosh S, Dellibovi-Ragheb TA, Kerviel A, Pak E, Qiu Q, Fisher M, et al. β -Coronaviruses use lysosomes for egress instead of the biosynthetic secretory pathway. *Cell.* 2020; 183(6):1520–35. e14. <https://doi.org/10.1016/j.cell.2020.10.039> PMID: 33157038
49. Hayn M, Hirschenberger M, Koepke L, Nchioua R, Straub JH, Klute S, et al. Systematic functional analysis of SARS-CoV-2 proteins uncovers viral innate immune antagonists and remaining vulnerabilities. *Cell Rep.* 2021; 35(7):109126. Epub 2021/05/12. <https://doi.org/10.1016/j.celrep.2021.109126> PMID: 33974846; PubMed Central PMCID: PMC8078906.
50. Chen D, Zheng Q, Sun L, Ji M, Li Y, Deng H, et al. ORF3a of SARS-CoV-2 promotes lysosomal exocytosis-mediated viral egress. *Dev Cell.* 2021. <https://doi.org/10.1016/j.devcel.2021.10.006> PMID: 34706264
51. Kumar S, Javed R, Mudd M, Pallikkuth S, Lidke KA, Jain A, et al. Mammalian hybrid pre-autophagosomal structure HyPAS generates autophagosomes. *Cell.* 2021. <https://doi.org/10.1016/j.cell.2021.10.017> PMID: 34741801
52. Zhang Y, Chen Y, Li Y, Huang F, Luo B, Yuan Y, et al. The ORF8 protein of SARS-CoV-2 mediates immune evasion through down-regulating MHC-. *Proc Natl Acad Sci U S A.* 2021;118(23).
53. Stukalov A, Girault V, Grass V, Karayel O, Bergant V, Urban C, et al. Multilevel proteomics reveals host perturbations by SARS-CoV-2 and SARS-CoV. *Nature.* 2021; 594(7862):246–252. <https://doi.org/10.1038/s41586-021-03493-4> PMID: 33845483

54. Sadowski L, Pilecka I, Miaczynska M. Signaling from endosomes: location makes a difference. *Exp Cell Res.* 2009; 315(9):1601–9. Epub 2008/10/22. <https://doi.org/10.1016/j.yexcr.2008.09.021> PMID: 18930045.
55. Zanin N, Viaris de Lesegno C, Lamaze C, Blouin CM Interferon Receptor Trafficking and Signaling: Journey to the Cross Roads. *Front Immunol.* 2020; 11:615603. Epub 2021/02/09. <https://doi.org/10.3389/fimmu.2020.615603> PMID: 33552080; PubMed Central PMCID: PMC7855707.
56. Majer O, Liu B, Kreuk LS, Krogan N, Barton GM. UNC93B1 recruits syntenin-1 to dampen TLR7 signaling and prevent autoimmunity. *Nature.* 2019; 575(7782):366–370. <https://doi.org/10.1038/s41586-019-1612-6> PMID: 31546246
57. Asselin-Paturel C, Trinchieri G. Production of type I interferons: plasmacytoid dendritic cells and beyond. *J Exp Med.* 2005; 202(4):461–5. Epub 2005/08/17. <https://doi.org/10.1084/jem.20051395> PMID: 16103406; PubMed Central PMCID: PMC2212850.
58. Nguyen TH, Liu X, Su ZZ, Hsu AC, Foster PS, Yang M. Potential Role of MicroRNAs in the Regulation of Antiviral Responses to Influenza Infection. *Front Immunol.* 2018; 9:1541. Epub 2018/07/20. <https://doi.org/10.3389/fimmu.2018.01541> PMID: 30022983; PubMed Central PMCID: PMC6039551.
59. Zhu X, He Z, Yuan J, Wen W, Huang X, Hu Y, et al. IFITM3-containing exosome as a novel mediator for anti-viral response in dengue virus infection. *Cell Microbiol.* 2015; 17(1):105–118. <https://doi.org/10.1111/cmi.12339> PMID: 25131332
60. Besse B, Charrier M, Lapiere V, Dansin E, Lantz O, Planchard D, et al. Dendritic cell-derived exosomes as maintenance immunotherapy after first line chemotherapy in NSCLC. *Oncoimmunology.* 2016; 5(4):e1071008. ARTN e1071008 <https://doi.org/10.1080/2162402X.2015.1071008> WOS:000374194200004. PMID: 27141373
61. Dai S, Wei D, Wu Z, Zhou X, Wei X, Huang H, et al. Phase I clinical trial of autologous ascites-derived exosomes combined with GM-CSF for colorectal cancer. *Mol Ther.* 2008; 16(4):782–90. Epub 2008/03/26. <https://doi.org/10.1038/mt.2008.1> PMID: 18362931; PubMed Central PMCID: PMC7106337.
62. Nassar W, El-Ansary M, Sabry D, Mostafa MA, Fayad T, Kotb E, et al. Umbilical cord mesenchymal stem cells derived extracellular vesicles can safely ameliorate the progression of chronic kidney diseases. *Biomater Res.* 2016; 20(1):1–11. <https://doi.org/10.1186/s40824-016-0068-0> PMID: 27499886
63. Wüst S, Schad P, Burkart S, Binder MJC. Comparative Analysis of Six IRF Family Members in Alveolar Epithelial Cell-Intrinsic Antiviral Responses. *Cell.* 2021; 10(10):2600. <https://doi.org/10.3390/cells10102600> PMID: 34685580
64. Cheng A, Negro C, Bruhn JF, Rice WJ, Dallakyan S, Eng ET, et al. Leginon: New features and applications. *Protein Sci.* 2021; 30(1):136–50. Epub 2020/10/09. <https://doi.org/10.1002/pro.3967> PMID: 33030237; PubMed Central PMCID: PMC7737759.
65. Suloway C, Pulokas J, Fellmann D, Cheng A, Guerra F, Quispe J, et al. Automated molecular microscopy: the new Leginon system. *J Struct Biol.* 2005; 151(1):41–60. Epub 2005/05/14. <https://doi.org/10.1016/j.jsb.2005.03.010> PMID: 15890530.
66. Zheng SQ, Palovcak E, Armache J-P, Verba KA, Cheng Y, Agard DA. MotionCor2: anisotropic correction of beam-induced motion for improved cryo-electron microscopy. *Nat Methods.* 2017; 14(4):331–332. <https://doi.org/10.1038/nmeth.4193> PMID: 28250466
67. Mastronarde DN. Automated electron microscope tomography using robust prediction of specimen movements. *J Struct Biol.* 2005; 152(1):36–51. Epub 2005/09/27. <https://doi.org/10.1016/j.jsb.2005.07.007> PMID: 16182563.
68. Tegunov D, Cramer P. Real-time cryo-electron microscopy data preprocessing with Warp. *Nat Methods.* 2019; 16(11):1146–52. Epub 2019/10/09. <https://doi.org/10.1038/s41592-019-0580-y> PMID: 31591575; PubMed Central PMCID: PMC6858868.
69. Galaz-Montoya JG, Flanagan J, Schmid MF, Ludtke SJ. Single particle tomography in EMAN2. *J Struct Biol.* 2015; 190(3):279–90. Epub 2015/05/10. <https://doi.org/10.1016/j.jsb.2015.04.016> PMID: 25956334; PubMed Central PMCID: PMC4457691.
70. Bepler T, Morin A, Rapp M, Brasch J, Shapiro L, Noble AJ, et al. Positive-unlabeled convolutional neural networks for particle picking in cryo-electron micrographs. *Nat Methods.* 2019; 16(11):1153–60. Epub 2019/10/09. <https://doi.org/10.1038/s41592-019-0575-8> PMID: 31591578; PubMed Central PMCID: PMC6858545.
71. Mastronarde DN, Held SR. Automated tilt series alignment and tomographic reconstruction in IMOD. *J Struct Biol.* 2017; 197(2):102–13. Epub 2016/07/23. <https://doi.org/10.1016/j.jsb.2016.07.011> PMID: 27444392; PubMed Central PMCID: PMC5247408.
72. Dobin A, Davis CA, Schlesinger F, Drenkow J, Zaleski C, Jha S, et al. STAR: ultrafast universal RNA-seq aligner. *Bioinformatics.* 2013; 29(1):15–21. Epub 2012/10/30. <https://doi.org/10.1093/bioinformatics/bts635> PMID: 23104886; PubMed Central PMCID: PMC3530905.

73. Anders S, Pyl PT, Huber W. HTSeq—a Python framework to work with high-throughput sequencing data. *Bioinformatics*. 2015; 31(2):166–169. <https://doi.org/10.1093/bioinformatics/btu638> WOS:000347832300003. PMID: [25260700](https://pubmed.ncbi.nlm.nih.gov/25260700/)
74. Love MI, Huber W, Anders S. Moderated estimation of fold change and dispersion for RNA-seq data with DESeq2. *Genome Biol*. 2014; 15(12):550. Epub 2014/12/18. <https://doi.org/10.1186/s13059-014-0550-8> PMID: [25516281](https://pubmed.ncbi.nlm.nih.gov/25516281/); PubMed Central PMCID: PMC4302049.
75. Bray NL, Pimentel H, Melsted P, Pachter L. Near-optimal probabilistic RNA-seq quantification. *Nat Biotechnol*. 2016; 34(5):525–527. <https://doi.org/10.1038/nbt.3519> PMID: [27043002](https://pubmed.ncbi.nlm.nih.gov/27043002/)
76. Quinlan AR, Hall IM. BEDTools: a flexible suite of utilities for comparing genomic features. *Bioinformatics*. 2010; 26(6):841–2. Epub 2010/01/30. <https://doi.org/10.1093/bioinformatics/btq033> PMID: [20110278](https://pubmed.ncbi.nlm.nih.gov/20110278/); PubMed Central PMCID: PMC2832824.
77. Krämer A, Green J, Pollard J Jr, Tugendreich S. Causal analysis approaches in ingenuity pathway analysis. *Bioinformatics*. 2014; 30(4):523–530. <https://doi.org/10.1093/bioinformatics/btt703> PMID: [24336805](https://pubmed.ncbi.nlm.nih.gov/24336805/)